SPECIAL
PECAN
COLLECTION

An Evaluation of the Impact of Assimilating AERI Retrievals, Kinematic Profilers, Rawinsondes, and Surface Observations on a Forecast of a Nocturnal Convection Initiation Event during the PECAN Field Campaign

Samuel K. Degelia and Xuguang Wang

School of Meteorology, University of Oklahoma, Norman, Oklahoma

David J. Stensrud

Department of Meteorology and Atmospheric Science, The Pennsylvania State University, University Park, Pennsylvania

ABSTRACT

Numerical weather prediction models often fail to correctly forecast convection initiation (CI) at night. To improve our understanding of such events, researchers collected a unique dataset of thermodynamic and kinematic remote sensing profilers as part of the Plains Elevated Convection at Night (PECAN) experiment. This study evaluates the impacts made to a nocturnal CI forecast on 26 June 2015 by assimilating a network of atmospheric emitted radiance interferometers (AERIs), Doppler lidars, radio wind profilers, high-frequency rawinsondes, and mobile surface observations using an advanced, ensemble-based data assimilation system. Relative to operational forecasts, assimilating the PECAN dataset improves the timing, location, and orientation of the CI event. Specifically, radio wind profilers and rawinsondes are shown to be the most impactful instrument by enhancing the moisture advection into the region of CI in the forecast. Assimilating thermodynamic profiles collected by the AERIs increases midlevel moisture and improves the ensemble probability of CI in the forecast. The impacts of assimilating the radio wind profilers, AERI retrievals, and rawinsondes remain large throughout forecasting the growth of the CI event into a mesoscale convective system. Assimilating Doppler lidar and surface data only slightly improves the CI forecast by enhancing the convergence along an outflow boundary that partially forces the nocturnal CI event. Our findings suggest that a mesoscale network of profiling and surface instruments has the potential to greatly improve short-term forecasts of nocturnal convection.

1. Introduction

Convection initiation (CI) refers to the process in which an air parcel is successfully lifted to its level of free convection (LFC) and produces a precipitating updraft (Markowski and Richardson 2010). At night in the Great Plains of the United States, CI commonly contributes to a nocturnal maximum in summer precipitation (e.g., Surcel et al. 2010). Nocturnal CI in the Great Plains also leads to thunderstorms that produce all severe weather hazards (Grant 1995; Horgan et al. 2007), although hail and wind are the most common threats (Reif and Bluestein 2017). Past studies have shown that numerical weather prediction (NWP) models that employ convective

parameterizations often underpredict nocturnal convective events in the High Plains of the United States (Davis et al. 2006). Although various deficiencies have been resolved through the use of convection-resolving models (Weisman et al. 2008), many of the mechanisms that initiate convection at night remain problematic for NWP forecasts (e.g., Johnson and Wang 2017; Johnson et al. 2017; Stelten and Gallus 2017; Johnson et al. 2018).

Reif and Bluestein (2017) note that NWP models are often tuned specifically for features that initiate surface-based convection, whereas nocturnal CI tends to be initiated by features above the boundary layer (Corfidi et al. 2008). For example, the nocturnal low-level jet (LLJ), defined as a wind maximum occurring within the lowest kilometer of the atmosphere after sunset (Bonner 1968; Shapiro et al. 2016), commonly

Corresponding author: Samuel K. Degelia, sdegelia@ou.edu

contributes to the development of nocturnal convection through enhanced convergence at its terminus (Trier and Parsons 1993). However, various studies find that NWP models often fail to correctly forecast both the height and strength of the LLJ (Storm et al. 2009; Shin and Hong 2011; Smith et al. 2015; Johnson and Wang 2017; Johnson et al. 2017). Additionally, models can sometimes have difficulty in correctly simulating the elevated moist layer that is key to generating nocturnal CI. Peters et al. (2017) connect errors in mesoscale convective system (MCS) forecasts to moisture biases, and in the simulations with negative moisture biases the models produce errors in both CI timing and location due to the parcels requiring additional residence time within the lifting regions.

Assimilating kinematic and thermodynamic observations can improve many of the above issues related to forecasting nocturnal CI. Recently, Degelia et al. (2018) show improvements to a nocturnal CI forecast by assimilating conventional and radar observations. They find that assimilating these data enhances the buoyancy and convergence prior to CI, while the radar observations aid in suppressing spurious convection and erroneous outflow boundaries. However, the observations assimilated in Degelia et al. (2018) have become routinely assimilated in operational centers and their impacts are now relatively understood. This study expands upon the findings of Degelia et al. (2018) by evaluating the forecast impact of assimilating a novel dataset collected during the Plains Elevated Convection at Night (PECAN; Geerts et al. 2017) field campaign. The PECAN project seeks to better understand the processes responsible for nocturnal convection in the Great Plains with a focus on nocturnal CI, MCSs, atmospheric bores, and the LLJ (Geerts et al. 2017). The data collected during the field campaign included a network of thermodynamic and kinematic profilers similar to that recommended by the National Research Council (2009).

The observations assimilated here consist of atmospheric emitted radiance interferometers (AERIs; Turner and Löhnert 2014), Doppler wind lidars (e.g., Menzies and Hardesty 1989), radio wind profilers (e.g., Benjamin et al. 2004), high-frequency rawinsondes, and special surface data taken from fixed and mobile PECAN platforms. Assimilating similar datasets individually has been shown to improve convective-scale forecasts of various features (e.g., Kawabata et al. 2007; Wulfmeyer et al. 2006), although no known studies focus specifically on nocturnal CI. Most prior observation impact studies connect improved forecasts to modifications of the low-level moisture field. For example, Benjamin et al. (2004) and Kawabata et al. (2014) show that assimilating radio

wind profilers or Doppler lidars can lead to moisture improvements that increase the convective available potential energy. Hitchcock et al. (2016) also show midlevel moisture improvements, but from assimilating special rawinsonde observations collected during a field campaign. Similarly, Sobash and Stensrud (2015) demonstrate improved diurnal CI forecasts through the assimilation of surface mesonet observations that increase the moisture within the boundary layer. Until recently, previous studies that evaluate the impact of assimilating AERI profiles have only assimilated simulated observations (Hartung et al. 2011; Otkin et al. 2011). These works find that AERI data can also improve boundary layer thermodynamics. A recent study by Coniglio et al. (2019) shows that assimilating real, high-frequency AERI retrievals can lead to improvements, albeit nonsignificant, in short-term convective forecasts. However, the Coniglio et al. (2019) study only assimilates data from a single AERI, and for a short period (2–5 h) prior to CI. Therefore, we aim to expand upon previous works by assimilating data collected by multiple AERI platforms and over a longer period of assimilation.

This study focuses on the 26 June 2015 nocturnal CI event during PECAN. The CI of interest occurred near an elevated moist layer located just north of the intersection of the LLJ with a synoptic boundary. Such placement is commonly observed during nocturnal CI events in the Great Plains. This paper tests the hypothesis that assimilating a large network of many different PECAN observations can improve the simulation of both the elevated moist layer and the ascent mechanisms. In addition to evaluating the impact of assimilating the entire PECAN dataset, data denial experiments are presented to assess the relative impact of each observation type.

An overview of the 26 June 2015 CI is presented in section 2. Section 3 discusses the data, models, and methods we use to evaluate the impact of assimilating the PECAN observations on the CI case study. The assimilation and data denial results are found in section 4. An ingredients-based approach is applied in section 5 to better understand what aspects of the environment lead to the observation sensitivities for CI, and in section 6 the moisture and kinematic impacts discussed in the previous section are explored through diagnosing the data assimilation (DA) cycles. A final summary is found in section 7.

2. Overview of the 26 June 2015 nocturnal CI event

As an upper-level ridge deepened over the southwestern United States on 25 June 2015 (Fig. 1a), northwesterly flow developed above the central Great Plains. A surface
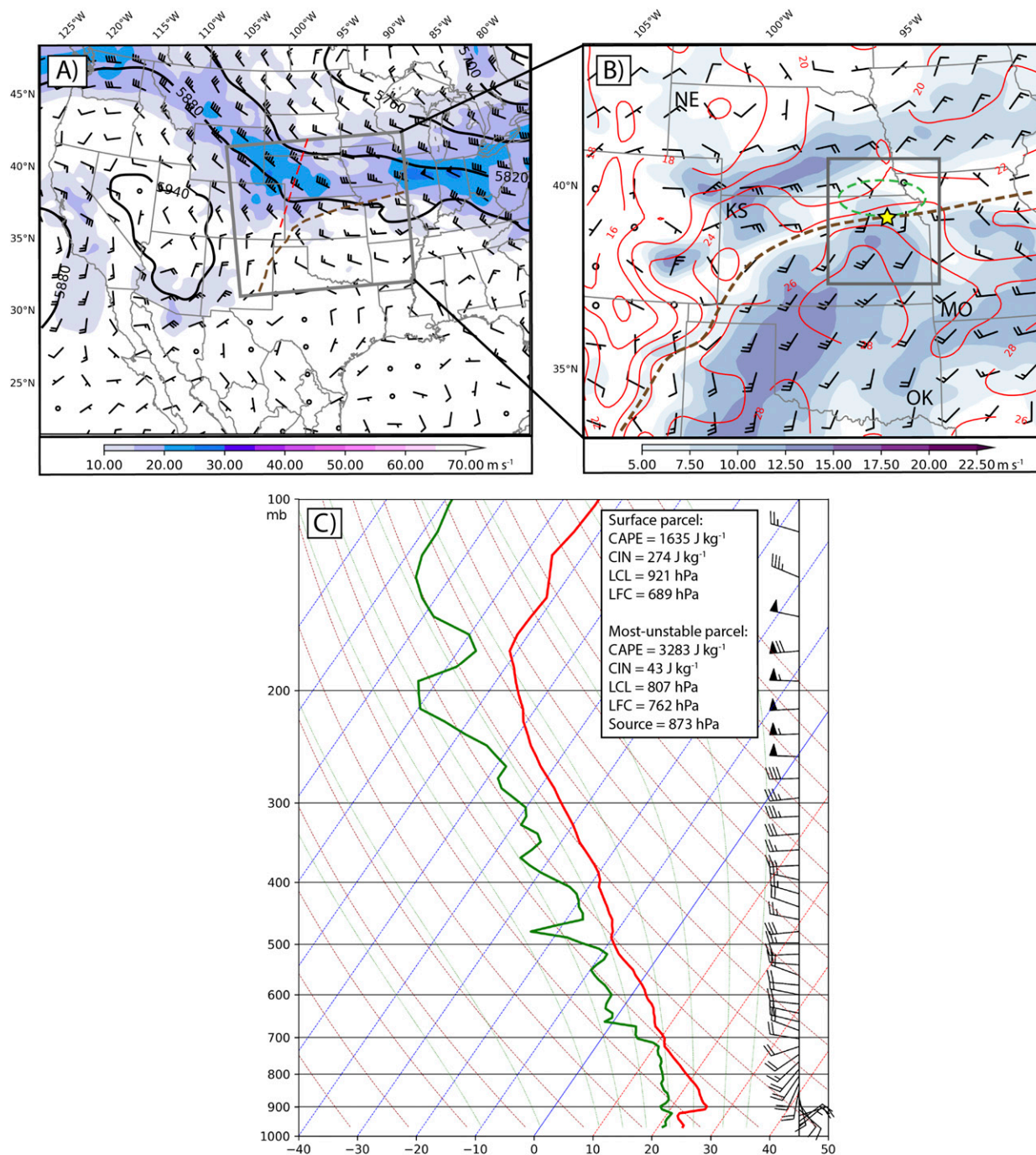
FIG. 1. Overview of the mechanisms leading to nocturnal CI on 26 Jun including (a) 500-hPa geopotential height (m; black contours) and winds (m s^{-1}; color fill and barbs) valid at 0300 UTC 26 Jun, (b) 850-hPa winds (m s^{-1}; color fill and barbs) and surface temperature contours (°C; red), and (c) a PECAN sounding taken from the location of the yellow star in (b) at 0215 UTC 26 Jun. In (a) and (b) the half barbs represent wind speeds of 2.5 m s^{-1} and the full barbs represent wind speeds of 5 m s^{-1}. The red dashed line in (a) represents the location of a shortwave trough axis, the brown dashed line in (a) and (b) represents the location of the synoptic boundary discussed in the text, and the dashed green circle in (b) indicates the approximate LLJ terminus. The plotting domains in (a) and (b) represent the outer and inner domains used for the simulations in this study, respectively. The gray box in (b) indicates the plotting domain for Fig. 8, below. The states of Kansas (KS), Nebraska (NE), Missouri (MO), and Oklahoma (OK) are also labeled in (b). The plots in (a) and (b) are created using model analyses from the Rapid Refresh model (Benjamin et al. 2016). The sounding in (c) is plotted using the quality-control checks provided by Loehrer et al. (1996). Except for the wind data being superob-ed to a depth of 20 hPa, the data in (c) are processed using the same methods described in the appendix.
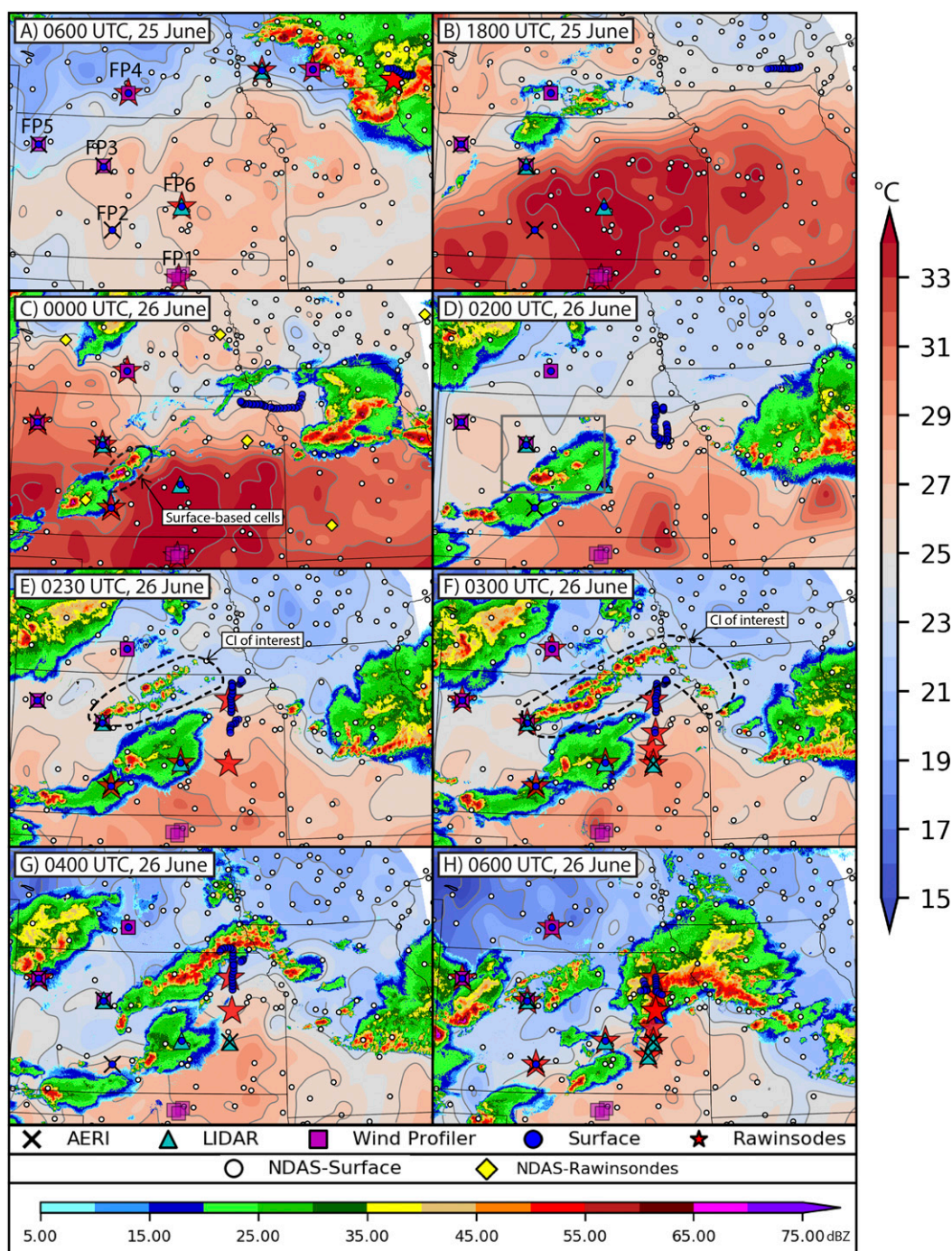
FIG. 2. Evolution of the 25–26 Jun nocturnal CI event in terms of composite reflectivity (dBZ; bottom color bar). The reflectivity data are provided by the MRMS (Smith et al. 2016). Additionally, an objective analysis of surface temperature (°C; right color bar) is shown using a two-dimensional linear spline interpolation. Surface temperature contours are also plotted in gray every 2°C. The observations in the objective analysis are obtained from the MesoWest program (Horel et al. 2002). The FP and MP PISAs are labeled in (a). Also overlaid are both the PECAN observations and conventional NDAS observations that are assimilated in this study. The circle in (c) indicates the location of two surface-based cells discussed in the text. The gray box shown in (d) indicates the plotting domain for Fig. 11, below. The circles in (e) and (f) indicate the nocturnal CI event of interest.
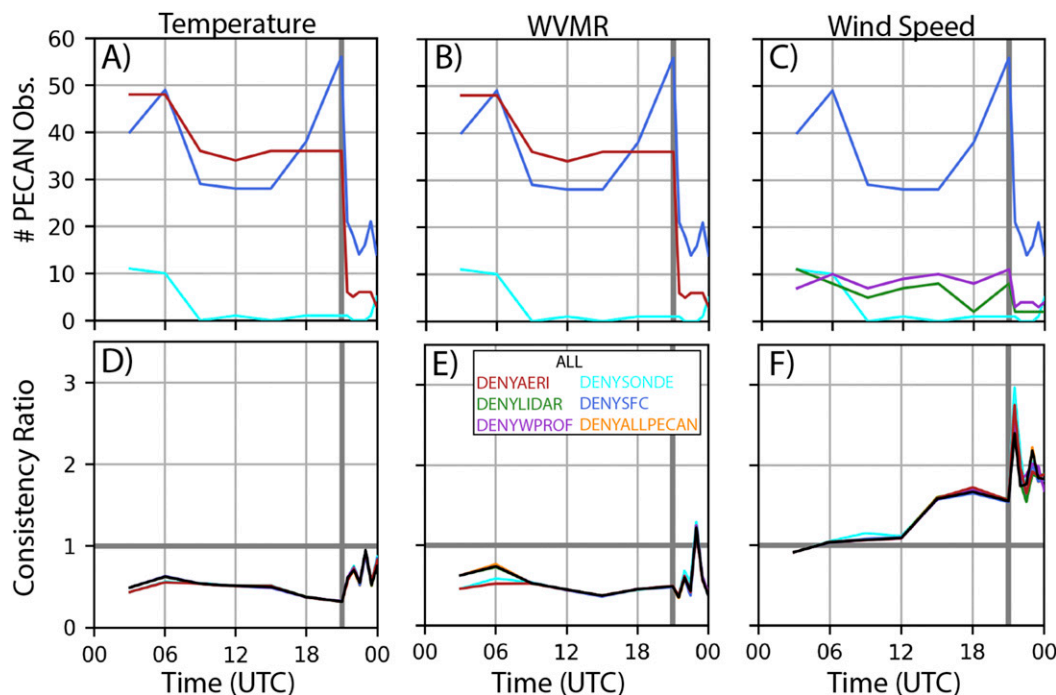
FIG. 3. Series of (a)–(c) the number of PECAN observations assimilated in the ALL experiment and (d)–(f) consistency ratio at each data assimilation cycle. The vertical gray lines indicate the transition from assimilating the PECAN observations on the outer domain (every 3 h) to assimilating them on the inner domain (every 10 min). The inner domain observation counts and consistency ratios (right of the vertical gray lines) are only plotted for every third cycle. The colors in (a)–(c) correspond to the observation type assimilated in ALL that was denied from its respective denial experiments labeled in (d)–(f). For example, the red line in (a)–(c) represents the number of AERI observations assimilated in ALL.

low, related to an embedded shortwave trough (Fig. 1a), strengthened a stalled, preexisting frontal boundary into a synoptic cold front (Figs. 1a,b). Additionally, a cold pool generated by early afternoon convection appears to have further reinforced this synoptic front (Fig. 2b). By the late afternoon of 25 June, stronger, surface-based cells developed along the synoptic boundary in central Kansas (Fig. 2c). After sunset at 0154 UTC (2054 LST), a southwesterly, criterion-1 LLJ (12.5 m s^{-1}; Bonner 1968) developed across western Oklahoma and central Kansas (Fig. 1b).

Conditions were favorable for further convective development after sunset on 25–26 June. First, large-scale isentropic ascent developed throughout northern Kansas due to the interaction of the LLJ with the synoptic boundary (Fig. 1b). Second, an additional mesoscale convergence zone associated with the northern terminus of the LLJ was present in northeastern Kansas (circled in Fig. 1b). At approximately 0215 UTC 26 June, a linear band of convective cells, which were disconnected from storms along the synoptic boundary, initiated in northern Kansas. These cells began to merge together with additional clusters of convection that developed in

northwestern Missouri (Fig. 2g). This arcing band of nocturnal convection (Figs. 2e,f) is the focal point of this study. The convective cluster continued to grow upscale into an MCS (Fig. 2h) that propagated southeastward, producing both severe wind and flash flooding throughout eastern Kansas. We note that many other nocturnal CI events occurred throughout Kansas on 26 June 2015, some of which are discussed in Trier et al. (2017).

Mobile observing platforms were deployed for this event as part of intensive observing period (IOP) 16. A sounding taken by a PECAN vehicle showed a moist layer atop the frontal inversion north of the synoptic boundary (Fig. 1c). Significant instability (>3000 J kg^{-1}) was associated with elevated air parcels, although some inhibition had to be overcome before CI could take place. As surface-based parcels were located below the frontal inversion, much of the nocturnal CI episode of interest was likely elevated. However, recent analyses of this event by Trier et al. (2018) and Sun and Trier (2018) highlight the potential role of outflow boundaries in the southern portion of the nocturnal CI event. In particular, the surface-based cells in Fig. 2c produced an outflow

TABLE 1. List of PECAN observing sites and instruments that are assimilated for the 26 Jun 2015 case study. Note that the FP1 site includes three wind profilers spaced by an average of 17 km.

Site name	Location	Instruments	Reference
FP1	Lamont, OK	915-MHz wind profiler (3)	Sivaraman et al. (1990)
		Rawinsonde	UCAR/NCAR (2015a)
FP2	Greensburg, KS	AERI	Turner (2016a)
		Rawinsonde	Vermeesch (2015)
		Surface obs	Delgado and Vermeesch (2016)
FP3	Ellis, KS	AERI	Turner (2016b)
		Doppler lidar	Hanesiak and Turner (2016a)
		449-MHz wind profiler	UCAR/NCAR (2017)
		Rawinsonde	Clark (2016)
		Surface obs	UCAR/NCAR (2015b)
FP4	Minden, NE	915-MHz wind profiler	UCAR/NCAR (2015c)
		Rawinsonde	UCAR/NCAR (2016a)
		Surface obs	UCAR/NCAR (2015b)
FP5	Brewster, KS	AERI	Turner (2016c)
		915-MHz wind profiler	UCAR/NCAR (2015d)
		Rawinsonde	UCAR/NCAR (2016b)
		Surface obs	UCAR/NCAR (2015b)
FP6	Hesston, KS	Doppler lidar	Hanesiak and Turner (2016b)
		Rawinsonde	Holdridge and Turner (2015)
		Surface obs	Turner (2016d)
MP1 "CLAMPS"	Mobile	Doppler lidar	Turner (2016e)
		Rawinsonde	Klein et al. (2016)
MP2 "MIPS"	Mobile	915-MHz wind profiler	Knupp and Wade (2016)
MP3 "SPARC"	Mobile	AERI	Wagner et al. (2016b)
		Doppler lidar	Wagner et al. (2016a)
		Rawinsonde	Wagner et al. (2016c)
		Surface obs	Wagner et al. (2016d)
MP4 "MISS"	Mobile	915-MHz wind profiler	UCAR/NCAR (2016c)
		Rawinsonde	UCAR/NCAR (2016d)
		Surface obs	UCAR/NCAR (2016c)
M-GAUS1	Mobile	Rawinsonde	Ziegler et al. (2016)
		Surface obs	Waugh and Ziegler (2017)
M-GAUS2	Mobile	Rawinsonde	Ziegler et al. (2016)
		Surface obs	Waugh and Ziegler (2017)
M-GAUS3	Mobile	Rawinsonde	Ziegler et al. (2016)
		Surface obs	Waugh and Ziegler (2017)
MM1	Mobile	Surface obs	Waugh and Ziegler (2017)
MM2	Mobile	Surface obs	Waugh and Ziegler (2017)
NSSL-NOXP	Mobile	Surface obs	Waugh and Ziegler (2017)

boundary that moved northward through the region of nocturnal CI and that will be discussed throughout this text. These findings indicate that some of the early cells in this CI event (Fig. 2e) were surface based.

3. Methods

a. Overview of the PECAN dataset

During PECAN, IOP observations were obtained from both fixed and mobile PECAN Integrated Sounding Arrays (PISAs). Each fixed (FP; Fig. 2a) and mobile PISA (MP) featured different instruments as described by Geerts et al. (2017). Data were also collected from separate mobile mesonetworks, mobile GPS Advanced Upper-Air Sounding Systems (MGAUS),

aircraft, and Doppler radar platforms. The PECAN observations assimilated in this study were collected during both IOP 15 (25 June) and IOP 16 (26 June) and varied throughout the assimilation period (Figs. 3a–c). These include AERIs [~5-min thermodynamic profiles produced by the AERIoe retrieval algorithm in Turner and Löhnert (2014)], Doppler lidars, radio wind profilers, rawinsondes, and surface observations (Table 1; Fig. 2). The PECAN observations were obtained from the PECAN field catalog (available online at http://catalog.eol.ucar.edu/pecan) in June 2018. Each instrument within a single dataset is provided in the same format and with the same level of quality control. The only exception is the radio wind profiler from FP3 that operated at 449 MHz, while the other radio wind
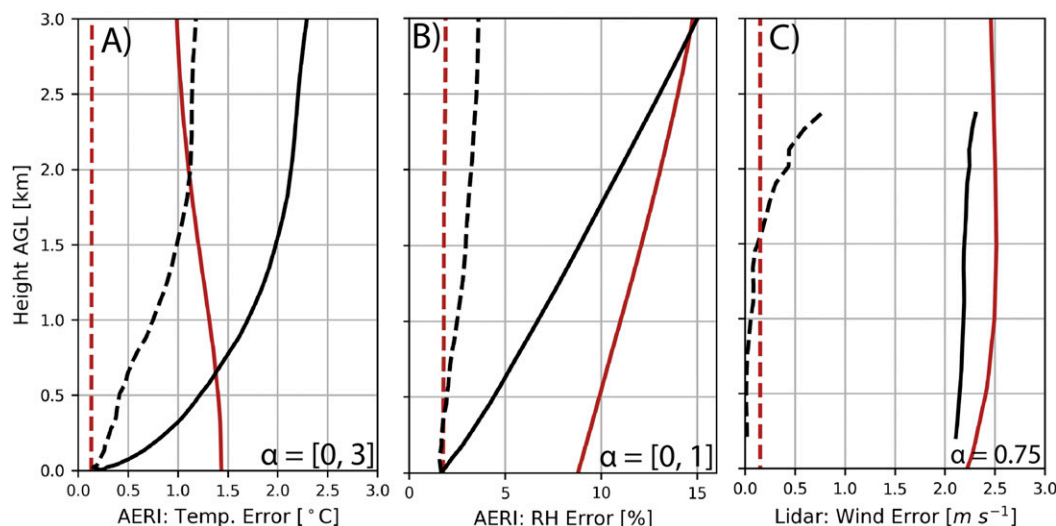
FIG. 4. Observation error profiles for (a) AERI temperatures (°C), (b) AERI moisture (% RH), and (c) Doppler lidar winds (m s^{-1}) used in Eq. (1). The plots are calculated by averaging each individual error profile associated with the respective AERI or Doppler lidar observations assimilated in this study. The red lines represent the rawinsonde instrument error obtained from Vaisala (2017) (σ_{Si}; dotted) and the static rawinsonde error from GSI (σ_{Sf}; solid). The black lines represent the input observation error profile provided by the PECAN dataset (σ_{Pi}; dotted) and the final observation error profile used for DA after inflation (σ_{Pf}; solid). The values used for α in Eq. (1) are also annotated for each variable. For AERI observation errors, the values of α vary linearly with height (from zero to the final bracketed value at 3 km AGL).

profilers operated at 915 MHz. We further preprocess each dataset following the methods described in the appendix. The large benefits from these meticulous preprocessing steps in the context of an MCS and bore are shown in Haghi et al. (2018).

We only assimilate vertical profiles of zonal and meridional wind (i.e., no radial velocity data) collected by the radio wind profilers and Doppler lidars. The radio wind profilers used during PECAN were composed of both 449- and 915-MHz profilers (Table 1). Except at FP3 (see Fig. 2a), the Doppler lidars were not collocated with radio wind profilers during PECAN. Thus, radio wind profilers and Doppler lidars could be considered complimentary for this case. However, differences in the design of the instruments could lead to different DA

impacts. Doppler lidars are only able to collect useful information from the lowest 1–3 km of the atmosphere due to the depth of potential scatterers (Menzies and Hardesty 1989). Doppler lidars also tend to sample finer-scale flow fields, such as turbulence, compared to radio wind profilers. Conversely, radio wind profilers collect backscatter from larger particles (e.g., hydrometeors, dust, and insects) that are present as high as 10 km above ground level (AGL).

The PECAN rawinsondes were launched more frequently than the operational network and at nonstandard times. During 25 June, both the FP and mobile sites collected rawinsonde data every 3 h. While rawinsondes are assimilated from fixed sites throughout the assimilation period, mobile rawinsondes (from MP and

TABLE 2. List of the physical parameterization schemes used for all simulations. A different microphysical parameterization scheme is used for the DA and forecast periods. Note that a cumulus parameterization scheme was not employed on the inner, 4-km domain.

Physical parameterization	Scheme	Reference
Microphysics (DA)	WRF single-moment 6-class (WSM6)	Hong and Lim (2006)
Microphysics (forecast)	Lin	Lin et al. (1983)
Planetary boundary layer	Mellor–Yamada–Nakanishi–Niino (MYNN)	Nakanishi and Niino (2006)
Longwave radiation	Rapid Radiative Transfer Model for general circulation models (RRTMG)	Iacono et al. (2008)
Shortwave radiation	Goddard	Tao et al. (2003)
Land surface model	Noah	Ek et al. (2003)
Cumulus	Grell–Freitas	Grell and Freitas (2013)

TABLE 3. Covariance localization radii used for each observation type assimilated for both the outer and inner domains. The horizontal localization radii are given in kilometers, and the vertical localization radii are given in scale height units (natural log of pressure).

Obs type	Horizontal localization radii (km; outer, inner)	Vertical localization radii [ln(p); outer, inner]
Conventional	700, 200	1.1, 0.55
Radar	—, 20	—, 0.55
AERI	700, 200	1.1, 0.55
Doppler lidar	700, 200	0.20, 0.20
Radio wind profiler	700, 200	0.20, 0.20
Surface (PECAN)	700, 200	1.1, 0.55
Rawinsonde (PECAN)	700, 200	1.1, 0.55

TABLE 4. List of experiments.

Expt name	Obs assimilated
DENYALL	Conventional and radar obs
ALL	Conventional, radar obs, and all PECAN obs listed in Table 1
DENYAERI	All obs from ALL except AERIs
DENYLIDAR	All obs from ALL except Doppler lidars
DENYWPROF	All obs from ALL except radio wind profilers
DENYSONDE	All obs from ALL except PECAN rawinsondes
DENYSFC	All obs from ALL except PECAN surface obs

MGAUS units) were only assimilated from IOP 15 prior to 0600 UTC 25 June. After 0600 UTC 25 June, rawinsonde data were collected from FP1 every 6 h. Because Privé et al. (2014) show significant improvements when assimilating rawinsondes more frequently, we expect the assimilation of PECAN rawinsondes here to produce a larger impact than those demonstrated by previous studies that only evaluate the operational network (e.g., Benjamin et al. 2010). We also note that the PECAN surface observations were collected more frequently than at operational sites (every 5 min at most PECAN platforms).

b. Treatment of observation errors for AERIs and Doppler lidars

In any DA algorithm, the observation error covariance matrix partially controls the weight between the observation and background states. When assimilating a new dataset, effort should be paid to how the observation errors are diagnosed (Bormann et al. 2011). Because radio wind profilers, rawinsondes, and surface observations are routinely assimilated in operational systems, we assimilate those PECAN observations using a preexisting, static error profile built into the Gridpoint Statistical Interpolation (GSI; Shao et al. 2016) software. Conversely, both AERIs and Doppler lidars are considered experimental and thus their observation errors are less understood. Luckily, both the AERIoe and lidar algorithms provide unique error profiles for each observing time using the methods in Turner and Löhnert (2014) and Newsom et al. (2017), respectively. Assimilating these novel observations with unique error profiles allows for less confident retrievals to have a lower weight in the analysis.

In addition to the instrument error, the observation errors used in a DA system should also include contributions from representativeness errors (Geer and Bauer 2011).

To account for the representativeness and any other residual errors, we inflate the AERI and lidar observation error profiles using

$$\sigma_{Pf}^2 = \sigma_{Pi}^2 + \alpha(\sigma_{Sf}^2 - \sigma_{Si}^2), \tag{1}$$

where σ_{Pi}^2 is the instrument observation error variance profile provided by the PECAN dataset and σ_{Pf}^2 is the final observation error variance profile used for DA. The $(\sigma_{Sf}^2 - \sigma_{Si}^2)$ term represents an initial estimate of the residual error profile for profiling instruments based on the difference between an instrument uncertainty profile for rawinsondes (σ_{Si}^2; provided by Vaisala 2017) and the full error profiles for assimilating rawinsondes in GSI (σ_{Sf}^2). The static error profiles in terms of σ_{Si} and σ_{Sf} are shown in red in Fig. 4. The initial estimate of residual error is then tuned using the parameter α that varied by instrument. The values of α are chosen by comparing the skill of nocturnal CI forecasts when varying α by intervals of 0.25. The selected values are annotated in Fig. 4. Through a trial-and-error process, we find improved forecasts when linearly increasing α with height for AERI observations, such that observation errors near the top of the profile are inflated more. We hypothesize that this is because the observations errors output by AERIoe only include the diagonal terms of its posterior error covariance matrix, whereas the off-diagonal terms are shown to increase with height in Turner and Löhnert (2014).

Example profiles of input and inflated observation errors for AERIs and Doppler lidars are shown in Fig. 4. Using this method, the forecast skill for the 26 June nocturnal CI event is improved compared to assimilating these observations using rawinsonde errors (not shown). Geer and Bauer (2011) and Minamide and Zhang (2017) use a similar approach to inflate observation error covariances for microwave imager radiances. This technique is only meant as a preliminary method for assimilating the AERI and Doppler lidar observations. In the future, we plan to further develop an optimal method for determining observation errors for these instruments.
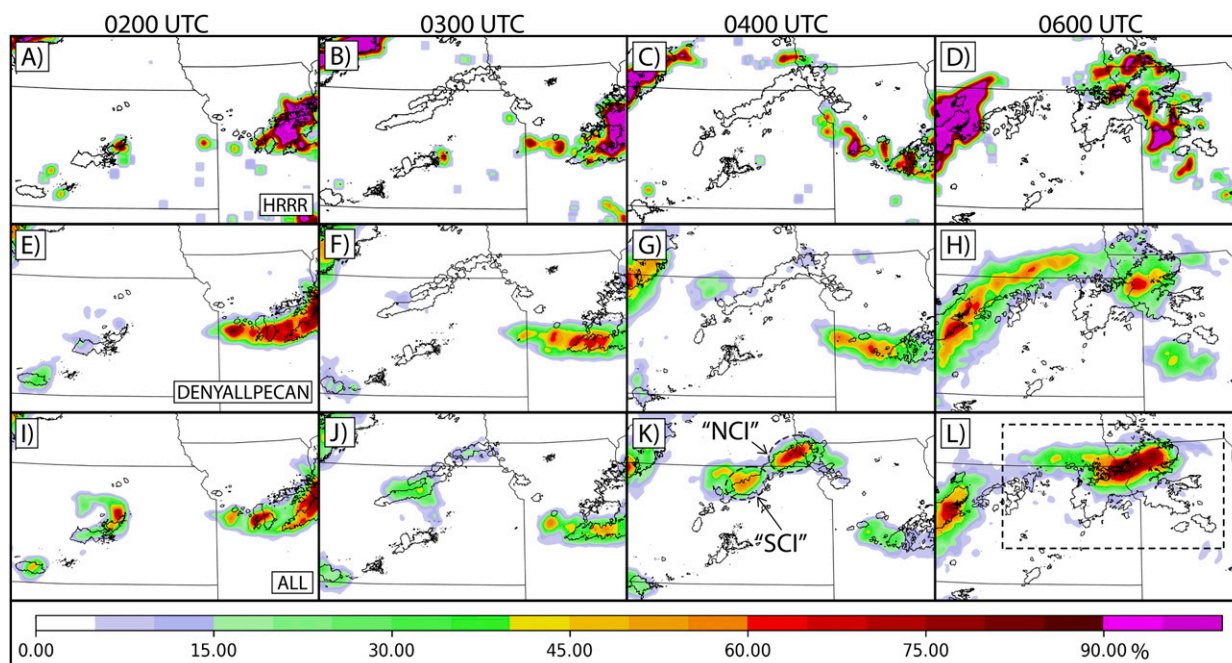
FIG. 5. Probability forecasts of composite reflectivity of >30 dBZ for (a)–(d) the operational HRRR forecast initialized at 0000 UTC 26 Jun, (e)–(h) the DENYALL experiment, and (i)–(l) the ALL experiment. The contours of observed composite reflectivity greater than 30 dBZ are also overlaid in black. The probabilities for (a)–(d) are calculated as the neighborhood probabilities with a radius of 8 km, and the probabilities in (e)–(l) are calculated as neighborhood ensemble probabilities with a radius of 8 km. The northern (NCI) and southern (SCI) initiation episodes are annotated in (k). The black box in (l) indicates the domain used to calculate the FSS shown in Fig. 6.

c. Design of the model and data assimilation system

The simulations presented in this study utilize version 3.7.1 of the Advanced Research version of the Weather Research and Forecasting (WRF) Model (WRF-ARW; Skamarock et al. 2008). There are 40 ensemble members configured on an outer, continental United States domain with 12-km grid spacing (shown in Fig. 1a). The ensemble members are initialized by downscaling members 1–20 of both the Global Ensemble Forecast System (GEFS; Wei et al. 2008) and Short-Range Ensemble Forecast (SREF; Du et al. 2014), following Johnson and Wang (2017) and Johnson et al. (2017). The native GEFS and SREF systems have horizontal resolutions of approximately 34 and 16 km, respectively. The GEFS and SREF members are also used to update the lateral boundary conditions on the outer domain. After DA is completed on the outer domain, an inner, convection-permitting domain with 4-km grid spacing is nested within the mesoscale grid (Fig. 1b). Both domains utilize 50 vertical levels on a stretched grid with a 50-hPa model top. The vertical grid spacing is approximately 200 m in the planetary boundary layer increasing to 450 m at 500 hPa. The physical parameterization schemes are fixed for each member following Degelia et al. (2018) and are listed in Table 2.

For DA, we apply an advanced, GSI-based ensemble Kalman filter (EnKF) system (Whitaker et al. 2008, Wang et al. 2013) extended for meso- and convective scales with direct radar data assimilation capabilities (Johnson et al. 2015; Wang and Wang 2017). The EnKF improves upon
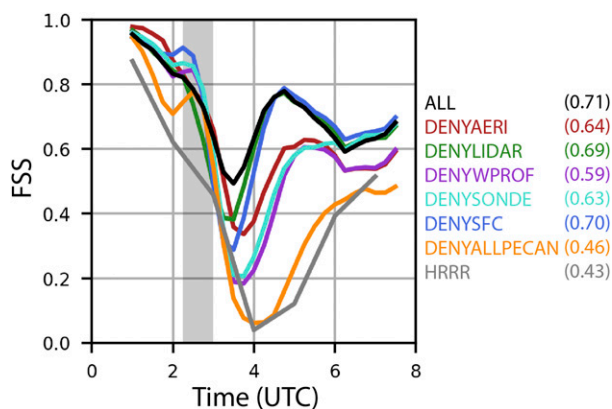

FIG. 6. Fractions skill score calculated with an 8-km neighborhood over the black box shown in Fig. 5l for a 2.54 mm h^{-1} precipitation threshold. The gray shading represents the approximate time of CI (between 0215 and 0300 UTC). The values shown in parentheses signify the FSS when averaged over the entire forecast period.
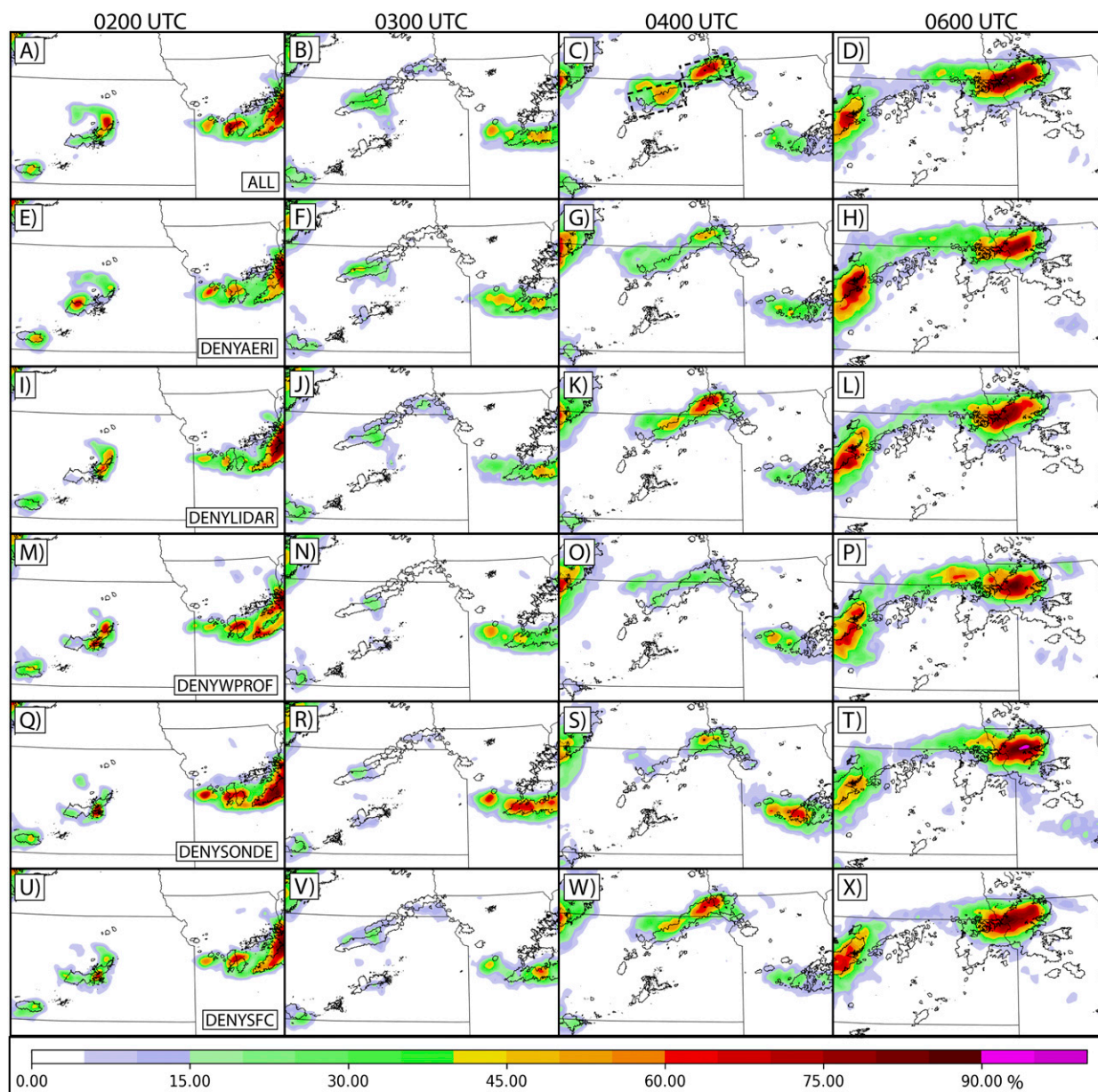
FIG. 7. Neighborhood ensemble probability forecasts for (a)–(d) ALL, (e)–(h) DENYAERI, (i)–(l) DENYLIDAR, (m)–(p) DENYWPROF, (q)–(t) DENYSONDE, and (u)–(x) DENYSFC. Each plot is calculated with a radius of 8 km. The dashed black boxes in (c) indicate the averaging regions for the profiles in Figs. 10–11, below.

other DA methods such as 3D-Var by sampling the background error covariance from ensemble forecasts (Johnson et al. 2015; Houtekamer and Zhang 2016). Because the 26 June event featured forcing mechanisms across a spectrum of scales (e.g., shortwave trough, LLJ, outflow boundary), a multiscale DA approach is used like that described in Degelia et al. (2018). Sensitivity tests are performed to determine the best covariance localization radii (Table 3) for each PECAN observation type described in the previous section. These settings are

tuned to produce the highest fractions skill score (FSS; discussed in section 4a) for the nocturnal CI event of interest. GSI applies an additional observation error inflation method when multiple observations are assimilated at the same location during the same DA cycle. By increasing the observation error and therefore reducing the observation information content, this method accounts for the observation error correlations when many observations from the same site are assimilated at the same time (e.g., high-frequency AERI
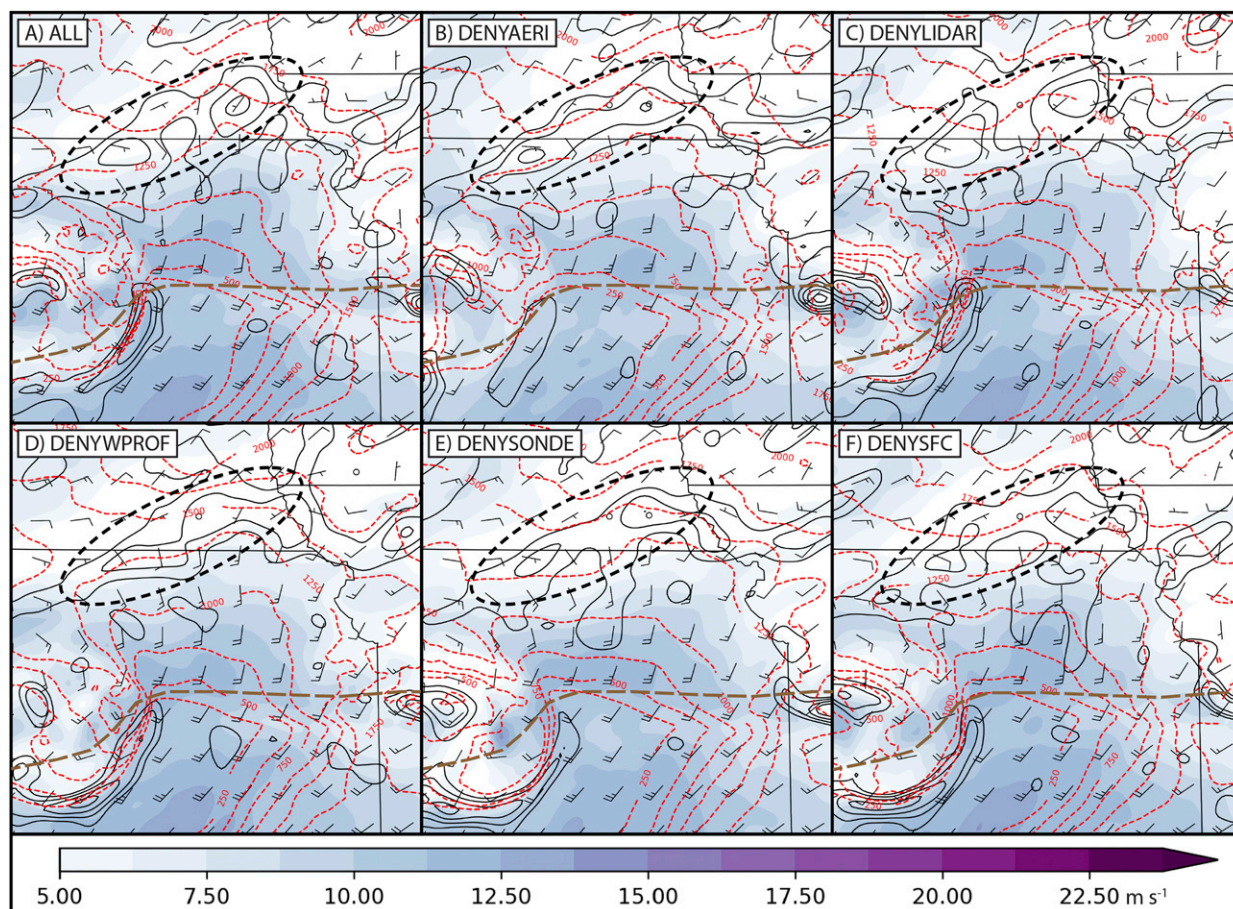
FIG. 8. Ensemble mean forecasts of 850-hPa winds (color fill; m s^{-1}) and convergence (contoured in black every $+5^{-6}$ s^{-1}) for (a) ALL, (b) DENYAERI, (c) DENYLIDAR, (d) DENYWPROF, (e) DENYSONDE, and (f) DENYSFC valid at 0200 UTC 26 Jun. The plotting domain is shown by the gray box in Fig. 1b. The half barbs represent wind speeds of 2.5 m s^{-1}, and the full barbs represent wind speeds of 5 m s^{-1}. Also overlaid in dashed red contours are the heights (every 250 m AGL) of the 312-K virtual potential temperature isentrope. The circled areas indicate the general location of the LLJ terminus corresponding to the CI event of interest, and the dashed brown lines indicate the approximate location of the synoptic boundary discussed throughout the text.

retrievals). See Degelia et al. (2018) for further discussion on the specific configuration of the GSI-based EnKF used, including an overview of covariance inflation parameters.

d. Experimental design and cycling description

To evaluate the impact of assimilating PECAN observations on the nocturnal CI forecast, we compare an experiment with all IOP observations assimilated (ALL) with a baseline forecast that only assimilates radar and conventional data ("DENYALLPECAN"). Additionally, we evaluate the relative forecast impact of each individual PECAN observation type through data denial experiments (Table 4). In the data denial framework, a decrease in forecast skill in a denial experiment indicates a positive impact when assimilating those specific observations. For the experiments here,

the observations are denied from the assimilation on both the outer and inner domain.

The cycling description that follows describes the ALL experiment. On the outer domain, conventional data are assimilated at 3-h intervals from 0000 to 2100 UTC 25 June. While the assimilation interval is 3 h, only observations from a 1-h time window (± 30 min centered on the analysis time) are assimilated on the outer domain. The conventional data are provided by the North American Mesoscale Forecast System Data Assimilation System (NDAS; Rogers et al. 2009) and include surface, rawinsonde, and ship and buoy observations (see Fig. 2). We choose to also assimilate PECAN observations on the outer, mesoscale domain with the same cycling configuration as the conventional observations. This is because elevated moist layers, which occur on the mesoscale and are often associated with
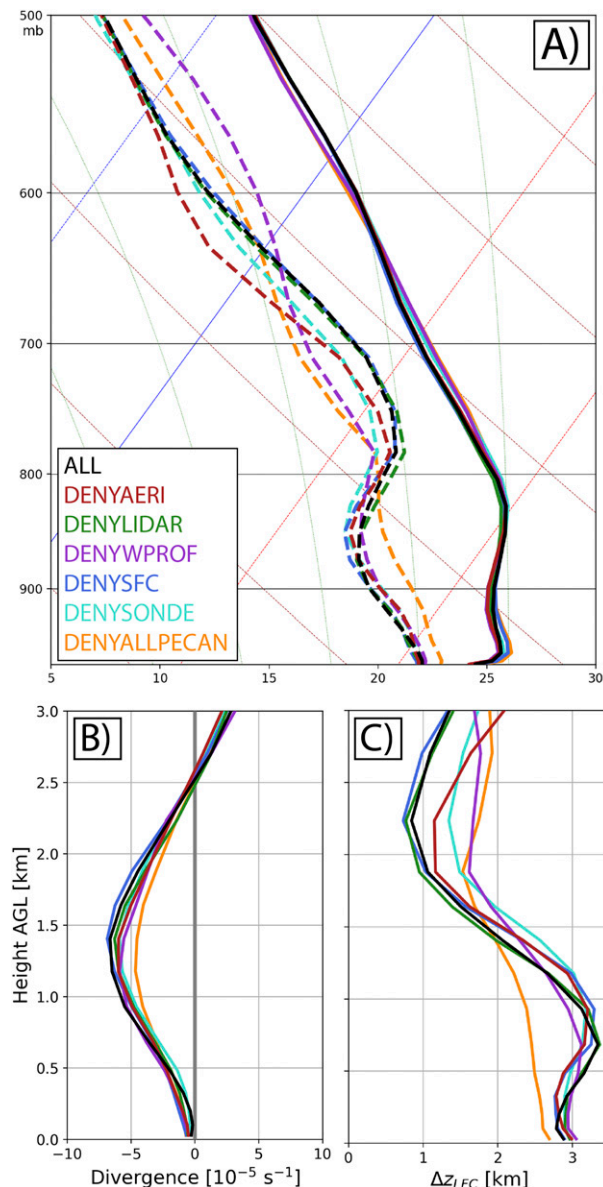
FIG. 9. (a) Profiles of temperature (solid lines) and dewpoint temperature (dashed lines), (b) divergence (10^{-5} s^{-1}), and (c) Δz_{LFC} (km) for each data denial experiment valid at 0200 UTC 26 Jun. The ensemble mean profiles are averaged over the northern black box in Fig. 7c.

instruments. The radar observations assimilated in this study (radar reflectivity factor and radial velocity) are preprocessed using the Warning Decision Support System–Integrated Information (WDSS-II; Lakshmanan et al. 2007). We assimilate the full radar dataset (i.e., no thinning) from all WSR-88D stations within the PECAN domain, following the methods described in Johnson et al. (2015) and Degelia et al. (2018). After the final DA cycle at 0000 UTC, 7.5-h forecasts are initialized from members 1–20 of the DA ensemble to cover the nocturnal CI event.

4. Overview of the forecast results when assimilating the PECAN dataset

Before discussing the forecast results from individual experiments, we present the consistency ratio (Dowell et al. 2004) for each experiment in Figs. 3d–f. The consistency ratio acts as an evaluation of the analysis system by calculating the ratio between the square of the total ensemble spread in observation space (Wheatley et al. 2014) and the root-mean-square innovation. A value of 1.0 indicates that the ensemble spread fully accounts for the background ensemble error, while values greater or less than 1.0 indicate overdispersion or underdispersion, respectively. During the outer domain DA cycles, the consistency ratio for thermodynamic variables remains less than one for each experiment (Figs. 3d–f), indicating that the ensemble spread is not sufficient to represent the background ensemble errors. After downscaling to the inner domain (Figs. 3d–f), the consistency ratios for the thermodynamic variables are closer to 1.0. For the wind speed, the ensembles are typically over-dispersive during both the outer and inner domain assimilation periods (Fig. 3f). Nevertheless, the ensemble statistics show no sign of filter divergence and each experiment produces generally similar values. Therefore, we assume that the DA system performs well enough for comparisons between the denial experiments.

a. Comparisons with an operational forecast of nocturnal CI

To first demonstrate the forecast impact of assimilating the PECAN dataset, we compare ALL and DENYALLPECAN with an operational forecast from the High-Resolution Rapid Refresh (HRRR; Earth System Research Laboratory 2016) model initialized at 0000 UTC 26 June. The forecast results from the HRRR are representative of other real-time simulations the 26 June nocturnal CI event. The experiments are first compared through raw neighborhood ensemble probability (NEP; Fig. 5) calculated using an 8-km neighborhood (Schwartz and Sobash 2017). Because the HRRR
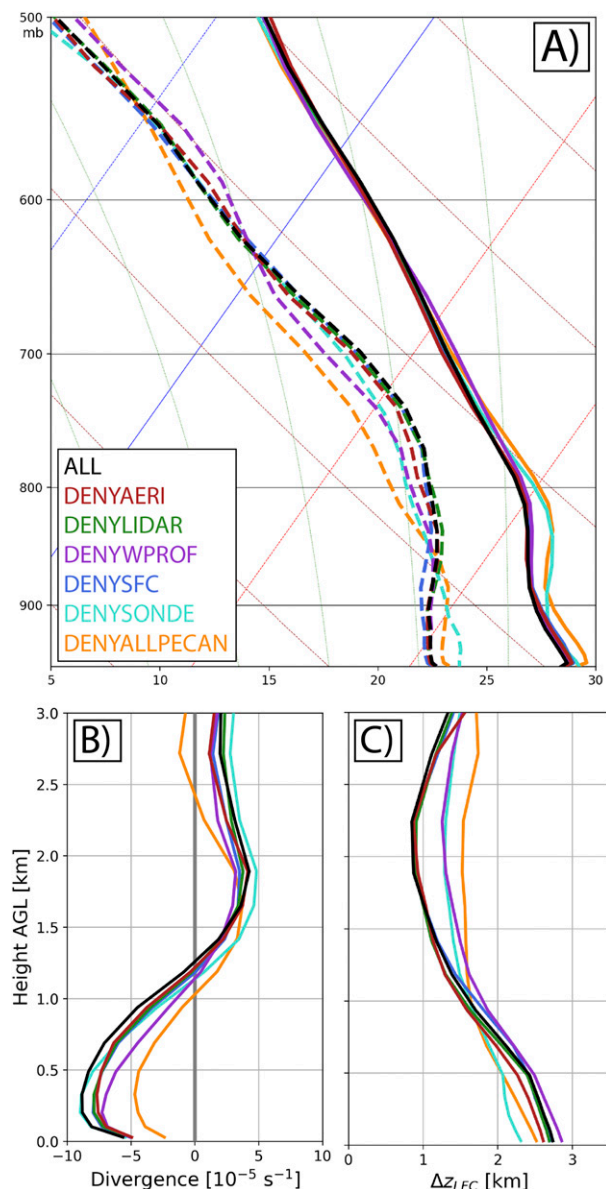
nocturnal CI (Wilson et al. 2018), could likely be improved by assimilating the thermodynamic profilers located at the FP sites. After 2100 UTC, the inner domain is initialized within the outer domain and conventional, PECAN, and level-2 Weather Surveillance Radar-1988 Doppler (WSR-88D) observations are assimilated at 10-min cycling intervals from 2110 UTC 25 June to 0000 UTC 26 June. Because the WSR-88D network sufficiently covers the domain of interest, we choose not to assimilate any special radar data collected by PECAN

FIG. 10. As in Fig. 9, but averaged over the southern black box in Fig. 7c. and valid at 0130 UTC 26 Jun.

is a deterministic forecast as opposed to ensemble-based, Figs. 5a–d are presented as neighborhood probabilities (NP), which are equivalent to the NEP calculated with a single ensemble member. Additionally, the forecasts are compared through a time series of FSS (Schwartz et al. 2010) calculated using 1-h accumulated precipitation data with a threshold of 2.54 mm h^{-1} (Fig. 6). The gridded precipitation data are provided by the Multi-Radar Multi-Sensor (MRMS) project at 1-km resolution before being interpolated onto our 4-km forecast domain (Zhang et al. 2016). The FSS is calculated over the box shown in Fig. 5l to ensure verification only over the

event of interest. By using NEP as the input for calculating FSS (Schwartz et al. 2010), the score represents an ensemble verification metric (FSS for the HRRR is calculated using NP instead).

Even though the nocturnal CI of interest was likely at least partially driven by the large-scale mechanisms discussed in section 2, the real-time HRRR simulations largely fail to capture the event (Figs. 5a–d). Between 0300 and 0400 UTC, the HRRR generates convection too far north and does not produce a southwest–northeast-oriented linear event as was observed. The FSS for the HRRR rapidly decreases from ~0.45 to 0.05 (Fig. 6) during this time period. While the simulations capture fairly well the convection forming in western Missouri (Figs. 5b,c), the HRRR only generates weak probabilities in southeastern Nebraska that fail to match the observed locations or orientation of the nocturnal CI event.

DENYALLPECAN demonstrates similar issues to those of the HRRR (Figs. 5e–h), and the FSS for the two forecasts are similar (Fig. 6). Again, the linear event is almost entirely missed apart from low probabilities of two convective events at the extreme ends of the line at 0400 UTC (Fig. 5g). These signals are not maintained and do not merge into a linear cluster. Eventually, DENYALLPECAN generates a new linear system, but it forms farther west than the observed event and is likely associated with a second CI event that is discussed in Trier et al. (2017). As the DENYALLPECAN experiment performs poorly and similar to the HRRR simulations, we assume that it serves as an accurate baseline to measure the advances that could be made when assimilating PECAN observations in an operational setting. We note that the lifting mechanisms discussed later are captured in both the HRRR and DENYALLPECAN (not shown). Thus, we hypothesize that the issues with these forecasts are primarily related to biases in the elevated instability profile.

Large forecast improvements are made when assimilating the IOP observations in ALL (Figs. 5i–l). The FSS for ALL first becomes larger than DENYALLPECAN at 0115 UTC (Fig. 6) due to improvements in resolving the ongoing surface-based convection in central Kansas. Shortly before 0300 UTC, ALL generates two distinct CI episodes along the northern and southern edge of observed linear event, henceforth called NCI (northern CI) and SCI (southern CI), respectively (Fig. 5k). By 0400 UTC, NCI and SCI congeal into a single linear event that closely matches the position and extent of the observed 30-dBZ contours (Fig. 5k). The linear convection in ALL then merges with additional convection in western Missouri to grow into a larger MCS, as was observed. Although the shape of the later MCS is not precisely
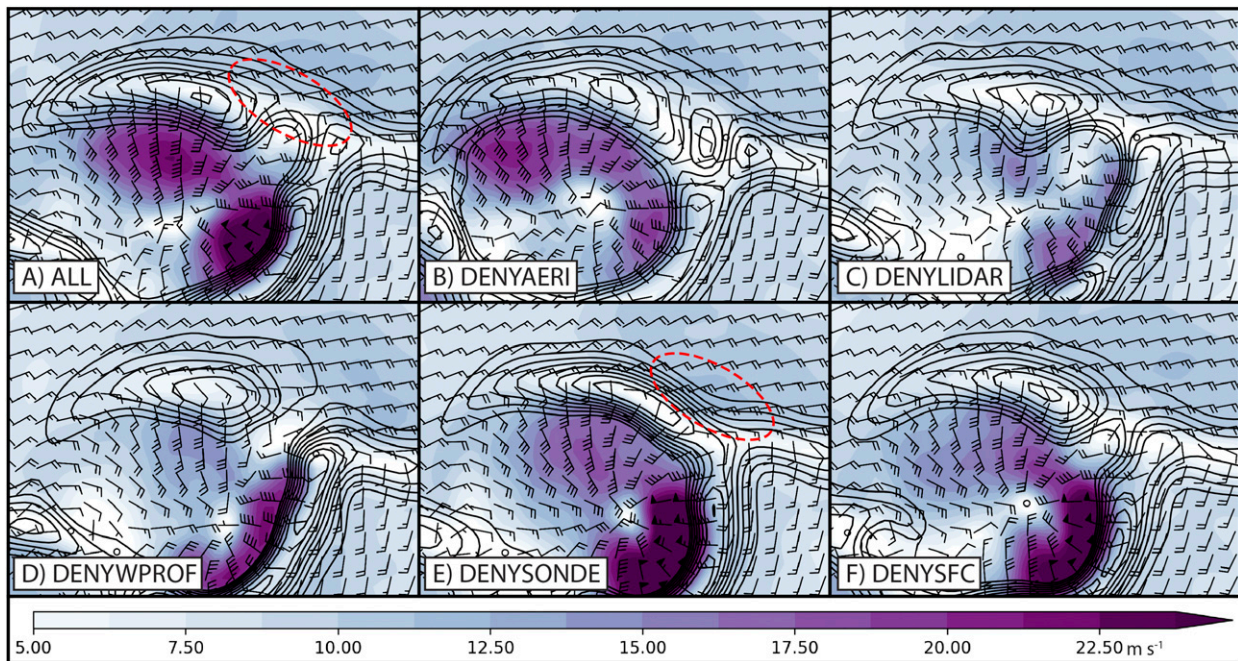
FIG. 11. Ensemble mean forecasts of 250 m AGL winds (color fill; m s^{-1}) and convergence (contoured in black every $+5^{-6}$ s^{-1}) for (a) ALL, (b) DENYAERI, (c) DENYLIDAR, (d) DENYWPROF, (e) DENYSONDE, and (f) DENYSFC valid at 0130 UTC 26 Jun. The plotting domain is shown by the gray box in Fig. 2d. The half barbs represent wind speeds of 2.5 m s^{-1}, and the full barbs represent wind speeds of 5 m s^{-1}. The plotting domain is zoomed into the outflow boundary produced by the ongoing surface-based cells discussed in the text. See the text for a description of the circled areas.

captured in ALL, the experiment correctly predicts a strongly organized MCS along the northern Kansas and Missouri border by 0600 UTC (Fig. 5l). Figure 6 demonstrates that after CI is simulated at 0300 UTC, ALL maintains higher skill than DENYALLPECAN throughout the entirety of the forecast.

b. Data denial experiments

Data denial experiments based on ALL are used to determine the relative impact of each individual PECAN observation type on the forecasts of SCI and NCI. The same NEP plots from Fig. 5 are presented for the denial experiments in Fig. 7, and the skill scores for each are shown in Fig. 6. Before discussing the experiments individually, note that ALL simulates NCI and SCI, as well as the upscale growth into an MCS, better than any denial experiment. The FSS is also higher in ALL than the other experiments shortly after CI (Fig. 6), indicating that all the individual observation types in the PECAN dataset have a positive impact on the CI forecast.

Prior to CI, "DENYAERI" performs slightly better than ALL (Fig. 6) due to it better capturing the decaying surface-based convection in central Kansas (Fig. 7e). However, large improvements from the assimilation of AERI observations appear shortly after 0300 UTC when ALL correctly begins to generate NCI in Nebraska

(Fig. 7b). DENYAERI does not produce the same convective cluster until 0330 UTC (not shown) and the FSS values are reduced from 0.50 in ALL to 0.35 in DENYAERI (Fig. 6). Because the convection within NCI eventually grows upscale into an MCS, DENYAERI also forecasts lower NEP values and produces a smaller MCS than ALL (Figs. 7d,h). These impacts are demonstrated in Fig. 6 as well, as the FSS for DENYAERI becomes lower than ALL after CI occurs and remains that way throughout the forecast period (Fig. 6). Thus, assimilating the AERI observations leads to a positive forecast impact for the northern cluster of CI and the later MCS.

Assimilating Doppler lidar observations has a smaller impact when compared with the other observation types evaluated in this study. "DENYLIDAR" forecasts NCI similar to ALL. The only apparent differences for NCI are that DENYLIDAR performs slightly better at capturing the additional convective events forming along the LLJ terminus in far western Missouri (Figs. 7b,j). Instead, DENYLIDAR shows a small decrease in skill around 0300 UTC (Fig. 6) that is primarily connected to the reduced probabilities and extent of SCI. At 0300 UTC, the maximum NEP values for SCI are reduced by ~15% in DENYLIDAR (Figs. 7b,j) compared to ALL. However, these differences in FSS do not
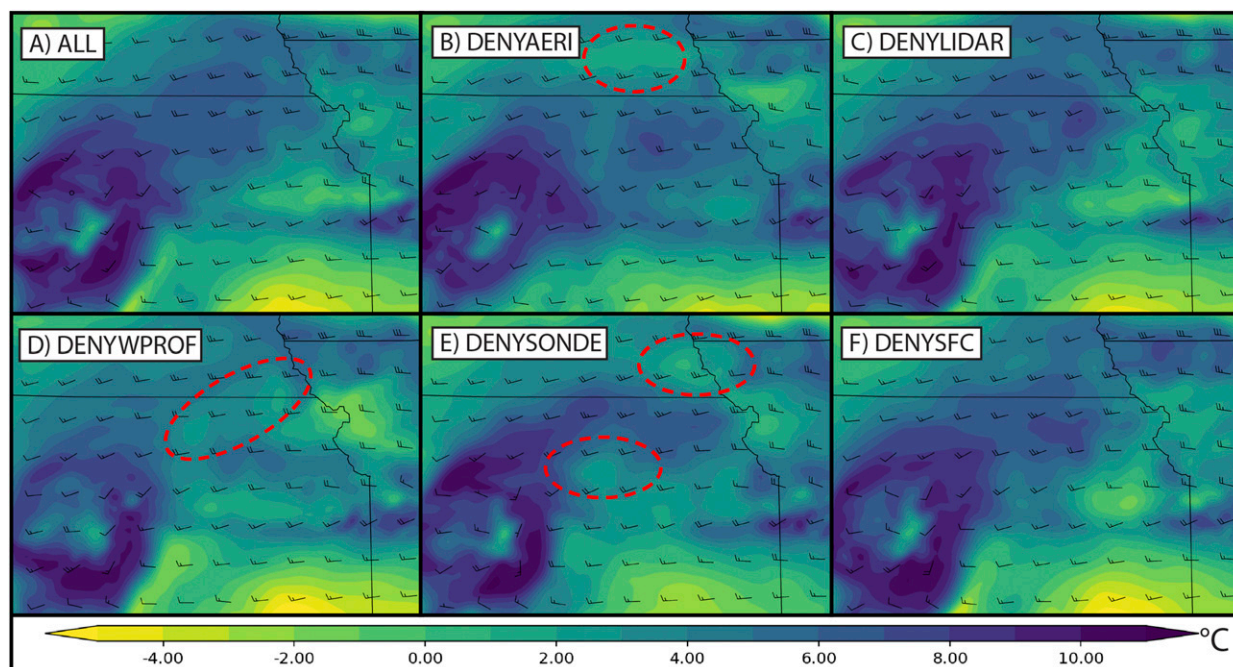
FIG. 12. Ensemble mean forecasts of 700-hPa dewpoint temperature (°C) and wind barbs for (a) ALL, (b) DENYAERI, (c) DENYLIDAR, (d) DENYWPROF, (e) DENYSONDE, and (f) DENYSFC valid at 0200 UTC 26 Jun. The half barbs represent wind speeds of $2.5\,\mathrm{m\,s^{-1}}$, and the full barbs represent wind speeds of $5\,\mathrm{m\,s^{-1}}$. See the text for a description of the red circles.

remain large after the convection grows upscale (Figs. 7d,l).

Similar to the AERI observations, assimilating radio wind profilers in ALL improves the forecast timing of NCI (Figs. 7b,n). Like DENYAERI, the convection that forms in southeastern Nebraska is not simulated by "DENYWPROF" until 0330 UTC (not shown). However, DENYWPROF also poorly captures SCI. Without assimilating the wind profiler data, the NEP values for SCI are reduced by nearly 40% relative to ALL at 0400 UTC (Figs. 7c,o). These large benefits are maintained throughout the upscale growth of the convective episodes into an MCS (Figs. 7d,p). DENYWPROF produces a lower FSS than any of the individual denial experiments after CI (Fig. 6), indicating that the radio wind profilers lead to the largest improvements compared with the rest of the PECAN dataset.

Assimilating the rawinsonde observations collected during PECAN produces a large improvement similar to that from the radio wind profilers. "DENYSONDE" simulates lower probabilities for both NCI and SCI relative to ALL at 0300 UTC (Figs. 7b,r). Additionally, DENYSONDE degrades the forecast for SCI at 0400 UTC (Fig. 7s) as the southern event is almost entirely missed. As in DENYWPROF, DENYSONDE also produces a large drop in FSS (Fig. 6) shortly after CI. Although the FSS for DENYSONDE converges with ALL (Fig. 6)

due to high ensemble probabilities (>90%) within the MCS, the extent of the MCS in DENYSONDE is still reduced compared to ALL. Therefore, the large improvements from assimilating rawinsonde observations are partially maintained throughout the later periods of the forecast.

Assimilating the special PECAN surface observations has a small benefit similar to those that result from assimilating the Doppler lidars. At early lead times, surface observations have a small, detrimental impact as seen by a higher FSS in "DENYSFC" relative to ALL at 0215 UTC (Fig. 6). These impacts again result from differences in how the DENYSFC experiment resolves the ongoing surface-based convection. Beginning at 0300 UTC (Figs. 7b,v), the positive impacts from assimilating the PECAN surface observations are mainly confined to SCI, as DENYSFC shows similar probabilities to DENYLIDAR. Again, these impacts from assimilating surface observations are small after the convection grows upscale, as the FSS from DENYSFC and ALL converge shortly after 0400 UTC (Fig. 6).

5. Ingredients-based analysis of the observation impacts

An ingredients-based approach (e.g., Johns and Doswell 1992) is used to determine which convective
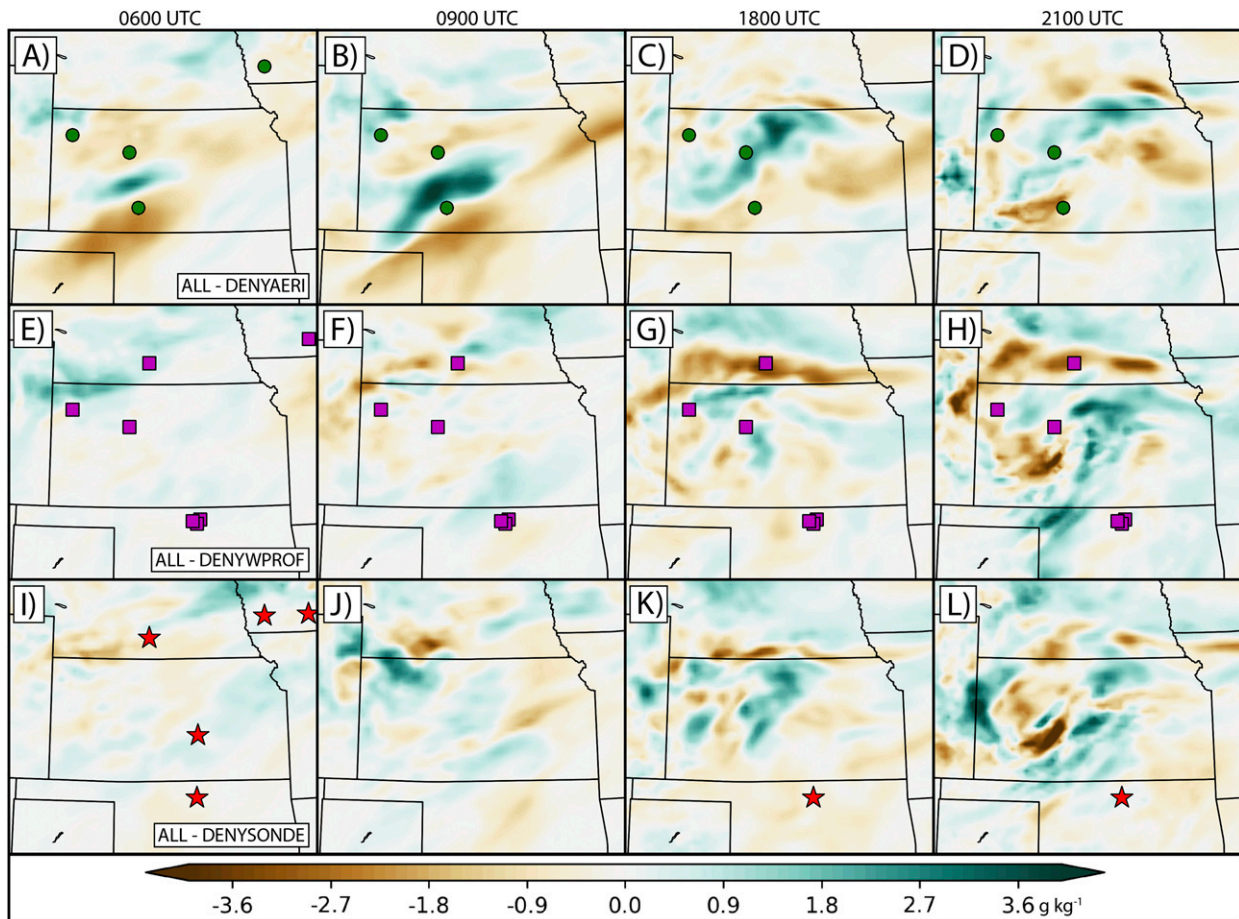
FIG. 13. Differences in analyzed ensemble mean water vapor mixing ratio ($g \, kg^{-1}$) between ALL and (top) DENYAERI at 700 hPa, (middle) DENYWPROF at 750 hPa, and (bottom) DENYSONDE at 750 hPa. The plots are valid at (a), (e), (i) 0600, (b), (f), (j) 0900, (c), (g), (k) 1800, and (d), (h), (l) 2100 UTC 25 Jun. Also overlaid are the locations of the AERIs [in (a)–(d); green dots], radio wind profilers [in (e)–(h); magenta squares], and PECAN rawinsondes [in (i)–(l); red stars] assimilated in ALL.

components (lift, moisture, instability) most contribute to the forecast impacts discussed in the previous section. By performing such an analysis, we determine exactly why certain observation types aid in the successful forecast of the 26 June nocturnal CI event.

a. Observation impacts on lifting mechanisms

We focus first on the lifting mechanisms responsible for the two individual CI clusters. Although the large-scale ascent mentioned in section 2 likely contributes to destabilization for parcels north of the synoptic boundary, additional mesoscale mechanisms are needed to lift the parcels to their LFC. For example, the observed sounding taken shortly before CI (Fig. 1c) shows that the most-unstable parcel, originating at 873 hPa, needed to be lifted to 762 hPa to reach its LFC (~1 km of lift). Analyses suggest that SCI forms along an outflow boundary produced by the surface-based convection along the synoptic front (as

hypothesized by Trier et al. 2018; see Fig. 2c). NCI initiates shortly afterward along the LLJ terminus (see Fig. 1b).

To first illustrate the large-scale, isentropic ascent, the heights of the 312-K virtual potential temperature θ_v isentrope are plotted (Fig. 8). In each simulation, the 312-K θ_v level is located at or just above the ground in east-central Kansas. The height of that same isentrope increases to the north as parcels are lifted isentropically above the synoptic boundary by the LLJ. Along the Kansas–Nebraska border and near the location of NCI, the 312-K isentrope is lifted to ~1250 m AGL in each experiment, demonstrating little observation impacts on the larger-scale ascent. Figure 8 also shows the horizontal mass convergence at 850 hPa over the LLJ terminus region for each data denial experiment. Again, no denial experiment has a large impact on the LLJ or the convergence located at its terminus. Although DENYWPROF and DENYSONDE simulate slightly weaker wind speeds just south of the jet
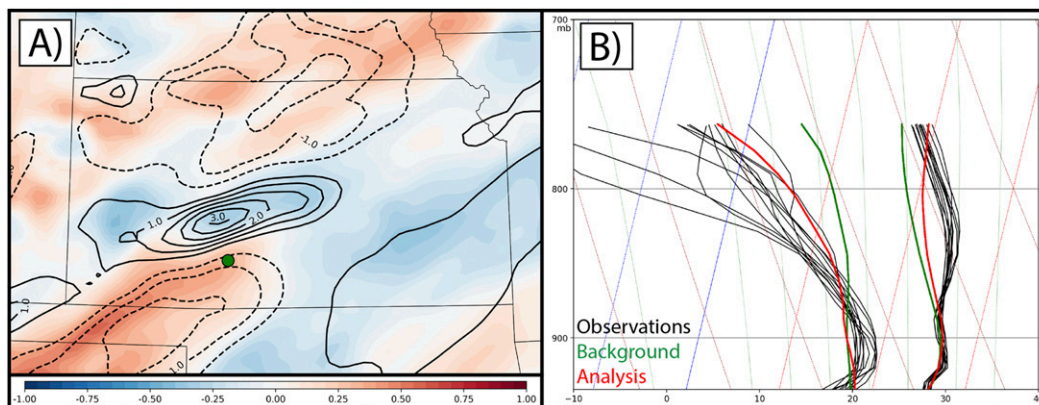
FIG. 14. (a) Background ensemble correlations between 750-hPa water vapor mixing ratio at FP2 (green dot) and 700-hPa water vapor mixing ratio across the domain, and (b) examples of all AERI profiles assimilated from FP2 (black lines) at 0600 UTC 25 Jun. The green lines indicate the ensemble mean of the background, and the red lines indicate the ensemble mean of the analysis. The rightmost cluster of lines in (b) represents the temperature (°C), and the leftmost cluster of lines represents the dewpoint temperature (°C). Also overlaid in (a) are the ensemble mean analysis increments (background minus analysis; black contours) for water vapor mixing ratio (g kg^{-1}). The dashed contours indicate negative increments, and the solid contours indicate positive increments. Both plots are taken from the ALL experiment.

terminus, those differences do not manifest in the convergence field. Because the ascent resulting from horizontal convergence is a function of the integrated convergence profile, vertical profiles are also shown in Fig. 9 (NCI) and 10 (SCI). Similar profiles of convergence are simulated by each experiment along the LLJ terminus and near NCI (Fig. 9b).

While the PECAN observations have little impact on forcing mechanisms for NCI, they have a larger impact on the convergence ahead of the outflow produced by the earlier surface-based convection (Figs. 10b and 11; see the first column of Fig. 7 for the forecasts of this surface-based convection). The wind speeds and convergence ahead of the cold pool are maximized at 250 m AGL (Fig. 10) and are shown in Fig. 11. Relative to ALL and DENYAERI (Figs. 11a,b), wind speeds in the northern section of the cold pool are over 8 m s^{-1} slower in DENYLIDAR, DENYWPROF, and DENYSFC (Figs. 11c–f). Due to the slower wind speeds south of this outflow boundary, the convergence profile along the boundary is weaker in those denial experiments (Fig. 10b). Although DENYSONDE simulates slower wind speeds within the cold pool compared to ALL (Fig. 11e), the experiment also enhances the winds ahead of the outflow boundary. Thus, DENYSONDE produces a similar magnitude of convergence as ALL for SCI (Figs. 11a,e and 10b). These convergence differences partially explain why assimilating the Doppler lidars, radio wind profilers, and surface observations aid in enhancing SCI. Without the additional ascent along the outflow boundary, parcels in DENYLIDAR, DENYWPROF, and DENYSFC need additional time to reach their LFC.

b. Observation impacts on the thermodynamic environment

Although assimilating the PECAN observations has little impact on the convergence near LLJ terminus, the denial experiments show large sensitivities to the elevated moist layer in the same area (Figs. 9a and 12). DENYAERI, DENYWPROF, and DENYSONDE, which all produce a large decrease in forecast skill for NCI, simulate drier midlevels near the LLJ terminus compared to ALL (Fig. 9a). The dry air in these three experiments leads to additional inhibition that needs to be eroded before parcels can reach their LFC. Another way of presenting the inhibition is through Δz_{LFC}, which describes the distance between a parcel's LFC and its starting height. The Δz_{LFC} parameter can be interpreted as the amount of lifting needed for a parcel to produce an accelerating updraft. In ALL, parcels originating at 2.25 km AGL near NCI need to be lifted only 900 m to reach their LFC. This value corresponds well with the sounding in Fig. 1c. Without AERI, radio wind profilers, or rawinsondes assimilated, these same parcels need to be lifted between 1200 and 1600 m (Fig. 9c). For SCI, only the assimilation of radio wind profilers or rawinsondes significantly modifies the thermodynamic environment (Figs. 10a,c). While assimilating both radio wind profilers and rawinsondes results in moister midlevels, the rawinsondes also strongly cool the layer between 900 and 800 hPa and thus further improve the
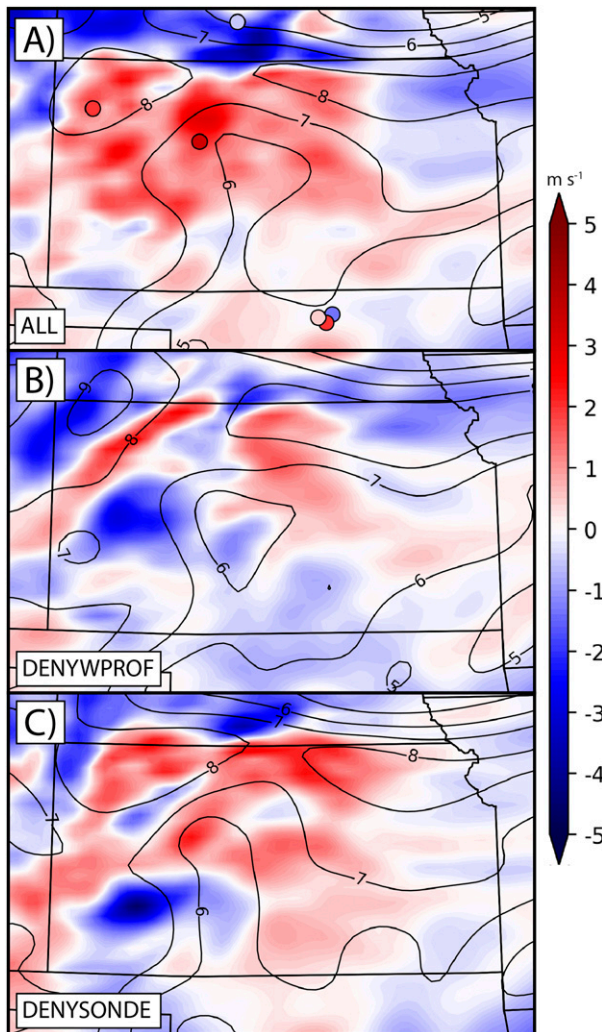
FIG. 15. Ensemble mean analysis increments (analysis minus background) of the 750-hPa zonal wind (m s^{-1}) for (a) ALL, (b) DENYWPROF, and (c) DENYSONDE valid at 1800 UTC 25 Jun. The black contours indicate the ensemble mean 750-hPa water vapor mixing ratio (g kg^{-1}) for each respective experiment. Also overlaid in (a) are the ensemble mean innovation values (observation minus background; dots) for the radio wind profiler observations closest to 750 hPa.

environment for SCI. In ALL, parcels originating at 2 km AGL for SCI need 900 m of lift to reach their LFC, while the same parcels in DENYWPROF or DENYSONDE need 1300 m of lift (Fig. 10c).

The impact on the elevated moist layer is further shown by the plan view plot in Fig. 12. Relative to ALL, the Doppler lidar and surface observations have little impact on the midlevel dewpoint temperatures throughout northern Kansas. When denying the AERI, radio wind profilers, or rawinsondes, however, the 700-hPa dewpoint temperatures are reduced by upward of 6°C in some locations. DENYWPROF and

DENYSONDE both modify the elevated moist layer over a large region that corresponds to both NCI and SCI (red circles in Figs. 12d,e). Conversely, the observation impacts from assimilating AERI observations are mainly confined to the region near the LLJ terminus corresponding to NCI (red circle in Fig. 12b).

6. Analysis of observation impacts on the data assimilation cycles

The previous section indicates that assimilating the PECAN observations enhances both the elevated moist layer (AERI, radio wind profilers, and rawinsondes) and the convergence along an outflow region produced by earlier, surface-based convection (Doppler lidars, radio wind profilers, and surface observations). These primary impacts likely lead to the improved forecast skill in ALL. However, it is not initially clear why, for example, assimilating the radio wind profilers modifies the moisture field. Thus, this final section of results explores the observation impacts throughout the DA cycles to briefly explain how the assimilation of PECAN observations impacts these important fields.

a. AERIs

Differences between the 700-hPa water vapor mixing ratio analyses for ALL and DENYAERI are presented in Figs. 13a–d. In ALL, most of the additional moisture from assimilating AERI observations originates on the outer domain DA cycles (0300–2100 UTC 25 June). At 0600 UTC 25 June, ALL shows increased moisture above the synoptic boundary compared to DENYAERI. The additional moisture is maximized at 700 hPa (Fig. 13a). By 0900 UTC, the moisture differences along the boundary in ALL reach nearly +4 g kg^{-1} (Fig. 13b). After 0900 UTC, the midlevel steering flow in ALL (see Fig. 12a) advects the additional moisture northeastward, eventually reaching the Kansas–Nebraska border by the final DA cycle on the outer domain (Fig. 13d). The region of additional moisture in ALL, compared to DENYAERI, correlates well with the location of NCI.

The additional moisture added above the synoptic boundary appears to be primarily related to negative increments in the midlevel moisture profile at FP2 (Fig. 14). First, the background ensemble in ALL indicates that the 750-hPa mixing ratio at the top of the AERI profiles from FP2 is negatively correlated with the elevated moist layer above the synoptic boundary (Fig. 14a; correlation calculated against 700-hPa mixing ratio where the impact is maximized). We hypothesize that this anticorrelation in the background is due to the ensemble indicating a strong moisture gradient along the frontal boundary, such that drier members at FP2 are
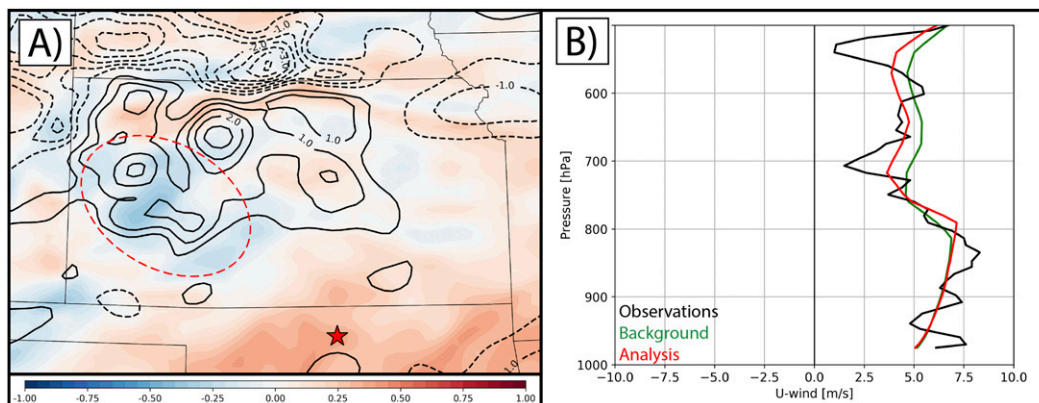
FIG. 16. (a) Background ensemble correlations between 700-hPa zonal wind at FP1 (red star) and 750-hPa zonal wind across the domain, and (b) the zonal wind profile assimilated from the FP1 rawinsonde at 1800 UTC 25 Jun. The green lines indicate the ensemble mean of the background, and the red lines indicate the ensemble mean of the analysis. Also overlaid in (a) are the ensemble mean analysis increments (background minus analysis; black contours) for zonal wind (m s^{-1}). The dashed contours indicate negative increments, and the solid contours indicate positive increments. Both plots are taken from the ALL experiment.

moister above the front. Next, the midlevels in the background are also 10°C too moist compared to corresponding AERI retrievals at FP2 (Fig. 14b). Therefore, while the AERI observations at FP2 aid in drying the midlevels in southwestern Kansas, the background covariance structure allows the same profiles to strongly moisten the midlevels above the synoptic boundary (Fig. 14a). This finding illustrates the primary advantage of using an ensemble-based DA method like the EnKF, as it can generate flow-dependent background error covariances.

b. Radio wind profilers and rawinsondes

As discussed earlier, assimilating the radio wind profilers in ALL results in additional moisture at 750 hPa throughout a large region of northeastern Kansas (Figs. 13e–h). This moisture primarily manifests during the final outer domain DA cycles between 1800 and 2100 UTC 25 June (Fig. 13h). However, unlike the assimilation of AERI observations, which directly add moisture, the additional moisture from assimilating radio wind profilers results from enhancements to the moisture advection field (Fig. 15). In northwestern Kansas, the 1800 UTC wind profiler observations at FP3 and FP5 produce innovations of +2–4 m s^{-1} in the zonal wind, which in turn, lead to a large, positive increment in ALL (Fig. 15a). Because most of the midlevel moisture is also located in northwestern Kansas (Fig. 15), the enhancement of the zonal wind in ALL increases the moisture advection into central and eastern Kansas. Without the assimilation of the wind profilers in DENYWPROF (Fig. 15b), the zonal wind decreases during the 1800 UTC cycle throughout much of western Kansas. Thus, DENYWPROF simulates weaker moisture advection

that eventually leads to the large differences in the 750-hPa moisture field at 2100 UTC (Fig. 13h).

As with the impact from assimilating radio wind profilers, the assimilation of rawinsonde data also leads to modifications to the midlevel zonal wind fields during the 1800 UTC cycle (Figs. 13k and 15c). However, only one rawinsonde was launched during this cycle while many wind profiles were collected throughout the domain (see Fig. 2b). The single rawinsonde assimilated at 1800 UTC from FP1 shows a large, negative innovation (~-3 m s^{-1}) between the observed and simulated zonal wind at 700 hPa (Fig. 16b). Because both the innovation at FP1 and correlations with the 750-hPa wind in western Kansas are negative (Fig. 16a), we deduce that assimilating the FP1 rawinsonde at 1800 UTC is at least partially responsible for the positive increment in the zonal wind shown in Fig. 15a. Therefore, in DENYSONDE, a negative increment in the zonal wind occurs in southwestern Kansas at 1800 UTC (Fig. 15c) that weakens the moisture advection into central Kansas. As in DENYWPROF, the weaker moisture advection then leads to reduced midlevel moisture during the later DA cycles in DENYSONDE compared to ALL (Figs. 13k,l).

c. Doppler lidars and surface observations

To determine why assimilating Doppler lidars or surface observations enhances the wind speeds within the outflow boundary, we analyze the common elements that contribute to stronger cold pools. We find little sensitivity to either the precipitation within the surface-based cells or the relative humidity profile below cloud base (not shown). Instead, when these observation types are assimilated near the ongoing surface-based convection,
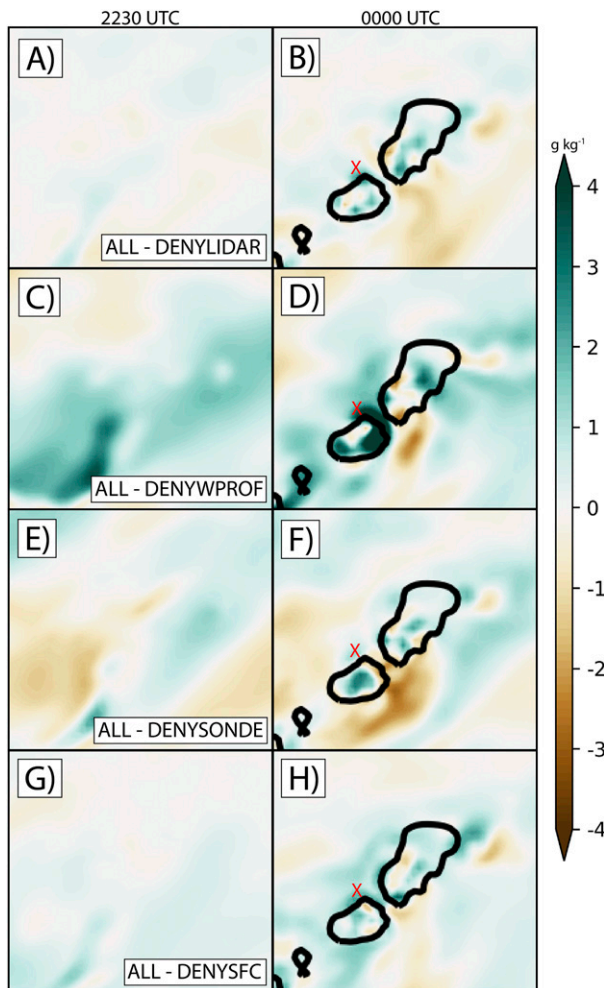
FIG. 17. As in Fig. 13, but for differences in ensemble mean water vapor mixing ratio (g kg^{-1}) at 650 hPa between ALL and (a),(b) DENYLIDAR; (c),(d) DENYWPROF; (e),(f) DENYSONDE; and (g),(h) DENYSFC. The plots are valid at (left) 2230 UTC 25 Jun and (right) 0000 UTC 26 Jun. Also overlaid are 15-dBZ contours of composite reflectivity from the ensemble mean of ALL. The red X in (b), (d), (f), and (h) indicates the location of the profile in Fig. 18.

convective-scale regions along the borders of the storms are moistened by the final assimilation cycle (Figs. 17b,h). This moisture impact is maximized at 600 hPa (Fig. 18). Assimilating wind profilers and rawinsonde observations produces similar effects near the ongoing convection (Figs. 17d,f), though additional moisture is already present due to the effects discussed previously. The additional moisture from assimilating Doppler lidar and surface observations does not exist prior to the development of the surface-based convection (Figs. 17a,g), indicating that the impacts are related to convective-scale DA. This impact extends throughout much of the midtroposphere, with DENYLIDAR and

DENYSFC simulating decreased dewpoint temperatures by an average of 2°–4°C between 500 and 800 hPa (Fig. 18). We hypothesize that the additional, convective-scale moisture added by these observations enhances the ongoing surface-based convection and later produces the stronger outflow seen only in ALL and DENYAERI (Fig. 9). Additionally, this increased moisture would likely reduce the impact of entrainment effects that could act to dissipate the ongoing convection.

7. Discussion and future work

By assimilating remote sensing profilers, high-frequency rawinsondes, and surface observations collected on 26 June, we find large improvements over a baseline experiment in terms of location, orientation, and timing of a nocturnal CI forecast. The most skillful forecast results occur when assimilating every PECAN dataset used in this study, thus indicating that each observation type plays a positive role in improving the CI forecast. Our results also suggest that the linear CI episode was initiated by two separate forcing mechanisms. NCI was initiated largely by the LLJ, while SCI formed along an outflow boundary produced by earlier, surface-based convection.

We conduct experiments within a data denial framework to evaluate the relative impact of assimilating each PECAN observation type within the full dataset. Assimilating AERI, radio wind profiler, and rawinsonde data produces the largest and most sustained impact due to enhancing the elevated moist layer in the region of CI. The radio wind profilers and rawinsondes affect both NCI and SCI by strengthening the moisture advection across northern Kansas. Assimilating AERI observations directly adds moisture above the synoptic boundary that is then advected into the NCI. This study is among the first to assimilate real AERI observations and demonstrates that high-frequency profiles of temperature and water vapor can improve short-term forecasts of convection. Additionally, the special rawinsondes assimilated here were launched more frequently and at nonstandard times relative to the operational network, thus providing further evidence for the value of assimilating high-frequency profiles.

The largest improvements result during DA cycling on the outer, mesoscale domain, indicating that assimilating profiler data can lead to forecast improvements even when not assimilating the data on a convection-permitting grid. However, additional improvements are found when assimilating the PECAN data at 4 km. When assimilating surface and Doppler lidar observations, the preexisting, surface-based convection produces
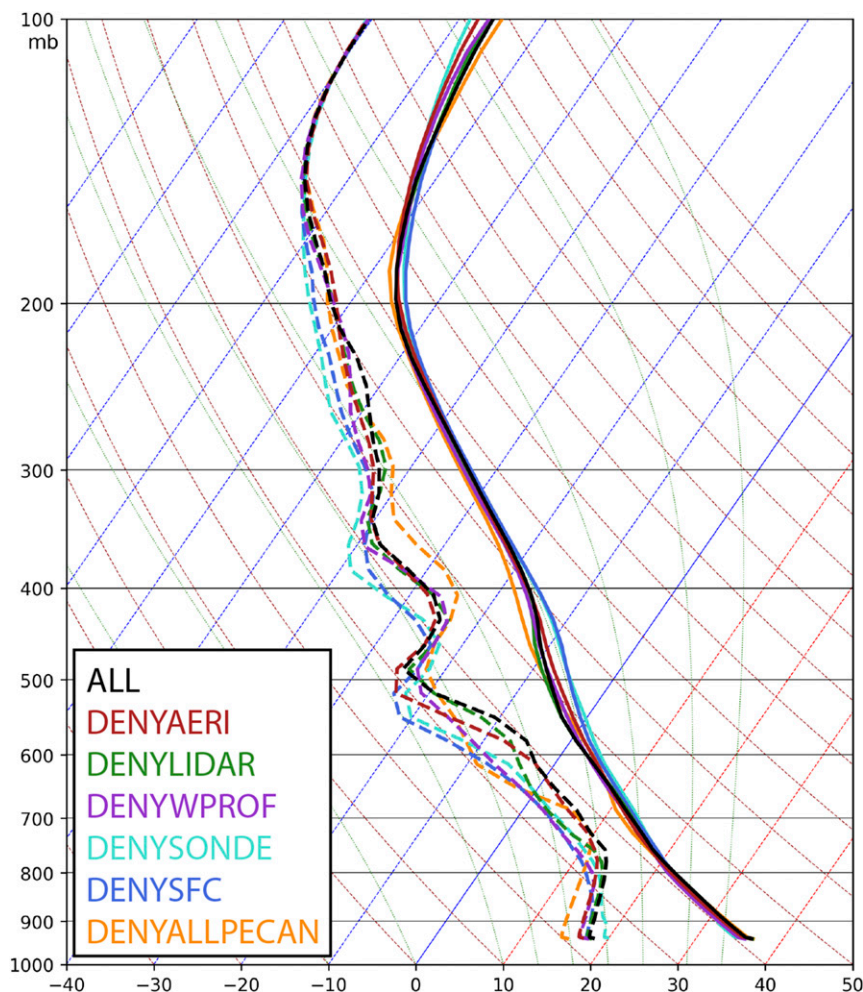
FIG. 18. Ensemble mean profiles of temperature (solid lines) and dewpoint temperature (dashed lines) taken from the red X in Fig. 17 and valid at 0000 UTC 26 Jun. The sounding is averaged over a neighborhood with a radius of two grid points (8 km).

a stronger outflow that enhances the ascent for the SCI. We hypothesize that the enhanced outflow is related to increased moisture near the analyzed convection that then enhances the ongoing storms during DA on the inner domain. Similar enhancements are also seen when assimilating the radio wind profiler observations. However, the improvements from assimilating surface and Doppler lidar observations diminish after the two simulated CI clusters merge into a larger MCS.

Still, various aspects of the results should be further explored. First, the location of each observation likely plays an important role on its impact. For example, the radio wind profilers assimilated here are possibly more impactful than Doppler lidars due to the additional radio wind profiler at FP4 (far northwestern Kansas site in Fig. 15a). An additional Doppler lidar at the same location could allow for a similar increment for the zonal

wind in northern Kansas. However, the higher maximum height of radio wind profilers (upward of 10 km AGL) also likely aids in the larger impact compared to Doppler lidars. Next, while we find an enhanced outflow boundary when assimilating Doppler lidar and surface observations, the impacts of convective-scale DA near ongoing convection is an area of research that has yet to be fully explored. Ensemble correlations near ongoing thunderstorms could be considered spurious due to the chaotic nature of convection. Thus, the impacts of assimilating the PECAN observations on the strength of the outflow boundary should be further studied.

For similar cases that show large thermodynamic errors, we expect that assimilating profiler observations can lead to improvements for short-term forecasts of CI. However, the strong forcing mechanisms for this event are captured well by each experiment, such that only the thermodynamic enhancements are needed for a

successful CI forecast. It is unclear whether assimilating such data could improve convergence mechanisms for other CI events, or if the observation impacts would be as large when the mechanisms are not well captured. As nocturnal convection can be initiated by many other features such as atmospheric bores or internal gravity waves, we plan to conduct a systematic evaluation of the impact of assimilating PECAN field observations on forecasts of nocturnal CI. To facilitate this work, a statistical method is also being developed to systematically quantify timing, location, and orientation errors for CI. By increasing our sample size using many CI cases from PECAN, we are verifying both the relative impact of each instrument type as well as the convective-scale impacts seen near the ongoing outflow boundary.

APPENDIX

Further Details and Preprocessing of the PECAN Dataset

The AERI instrument observes a "spectrally resolved downwelling radiance emitted by the atmosphere in the infrared portion of the electromagnetic spectrum" before retrieving a thermodynamic profile using an optimal-estimation retrieval technique [see Turner and Löhnert (2014, p. 752) for more details]. Because the retrieval accuracy quickly decreases with height and above cloudy layers, no observations above either 3 km AGL or cloud base are assimilated here (D. Turner 2016, personal communication). Additionally, to reduce

both the correlated and uncorrelated observation errors, a "superob" method (e.g., Berger 2004) is applied to each retrieval wherein the observations are averaged over a 10-hPa depth. For all observation types, we only apply the superob method to the portions of the profile for which the native observation spacing is less than the superob depth. We do not apply any temporal averaging or thinning techniques to the data, as one large advantage of the AERI is its ability to capture rapid changes in moisture and stability (Blumberg et al. 2017).

The vertical profiles from each wind profiler site are provided as 30-min averages. At FP4, FP5, and MP4, the wind profiles are calculated using the improved moments algorithm (Morse et al. 2002), which provides a confidence measure for each observation. We reject any data with a confidence below 0.5 as recommended by the data providers. At FP3, any 449-MHz wind profiler data with a signal-to-noise ratio of less than -6 dB are rejected (W. Brown 2018, personal communication). Furthermore, at FP4 and FP5, the 915-MHz profilers operate in both a "low" mode that features 180-m vertical sampling up to 4 km AGL and a "high" mode that features 360-m vertical sampling up to 12 km AGL. We choose to form a composite profile at these sites by rejecting any high-mode data below 4 km AGL. The superob method with a depth of 100 m (similar to a depth of 10 hPa in the boundary layer) is applied to these observations, because no pressure data are provided.

To remove the impacts of turbulence not resolved by the 4-km model and to be consistent with the averaging window for radio wind profilers, Doppler lidar observations are temporally averaged into 30-min profiles. Data below 100 m or above 3000 m AGL are not assimilated because of quality issues (D. Turner and P. Klein 2018, personal communications). We also perform gross checks to remove any erroneous databased on the root-mean-square difference between the observed radial velocity and its fitted values. Again, the wind observations are superobbed to a depth of 100 m.

The PECAN surface observations (temperature, humidity, wind, and pressure) are thinned to 5-min intervals due to the high frequency of the data. Other than gross checks for valid data, no other quality-control methods are applied to the surface observations before the assimilation.

The rawinsonde data are provided with quality-control markers following the methods described in Loehrer et al. (1996). Only the levels at which all data are marked as good are assimilated. The rawinsonde data are also superob-ed to a depth of 10 hPa to be consistent with the other PECAN observations.

REFERENCES

Benjamin, S. G., B. E. Schwartz, E. J. Szoke, and S. E. Koch, 2004: The value of wind profiler data in U.S. weather forecasting. *Bull. Amer. Meteor. Soc.*, **85**, 1871–1886, https://doi.org/10.1175/BAMS-85-12-1871.

——, B. D. Jamison, W. R. Moninger, S. R. Sahm, B. E. Schwartz, and T. W. Schlatter, 2010: Relative short-range forecast impact from aircraft, profiler, radiosonde, VAD, GPS-PW, METAR, and mesonet observations via the RUC hourly assimilation cycle. *Mon. Wea. Rev.*, **138**, 1319–1343, https://doi.org/10.1175/2009MWR3097.1.

——, and Coauthors, 2016: A North American hourly assimilation and model forecast cycle: The Rapid Refresh. *Mon. Wea. Rev.*, **144**, 1669–1694, https://doi.org/10.1175/MWR-D-15-0242.1.

Berger, H., 2004: Satellite wind superobbing. EUMETSAT Satellite Application Facility on Numerical Weather Prediction (NWP SAF) Doc. NWPSAF-MO-VS-016, 33 pp., https://www.ssec.wisc.edu/~howardb/Papers/superob_nwpsaf_final.pdf.

Blumberg, W. G., T. J. Wagner, D. D. Turner, and J. Correia, 2017: Quantifying the accuracy and uncertainty of diurnal thermodynamic profiles and convection indices derived from the Atmospheric Emitted Radiance Interferometer. *J. Appl. Meteor. Climatol.*, **56**, 2747–2766, https://doi.org/10.1175/JAMC-D-17-0036.1.

Bonner, W. D., 1968: Climatology of the low level jet. *Mon. Wea. Rev.*, **96**, 833–850, https://doi.org/10.1175/1520-0493(1968)096<0833:COTLLJ>2.0.CO;2.

Bormann, N., A. J. Geer, and P. Bauer, 2011: Estimates of observation-error characteristics in clear and cloudy regions for microwave imager radiances from numerical prediction models. *Quart. J. Roy. Meteor. Soc.*, **137**, 2014–2023, https://doi.org/10.1002/qj.833.

Clark, R., 2016: FP3 Ellis, KS radiosonde data, version 2.0. UCAR/NCAR–Earth Observing Laboratory, accessed 1 June 2018, https://doi.org/10.5065/D6GM85DZ.

Coniglio, M. C., G. S. Romine, D. D. Turner, and R. D. Torn, 2019: Impacts of targeted AERI and Doppler lidar wind retrievals on short-term forecasts of the initiation and early evolution of thunderstorms. *Mon. Wea. Rev.*, **147**, 1149–1170, https://doi.org/10.1175/MWR-D-18-0351.1.

Corfidi, S. F., S. J. Corfidi, and D. M. Schultz, 2008: Elevated convection and castellanus: Ambiguities, significance, and questions. *Wea. Forecasting*, **23**, 1280–1303, https://doi.org/10.1175/2008WAF2222118.1.

Davis, C. A., B. Brown, and R. Bullock, 2006: Object-based verification of precipitation forecasts. Part I: Methodology and application to mesoscale rain areas. *Mon. Wea. Rev.*, **134**, 1772–1784, https://doi.org/10.1175/MWR3145.1.

Degelia, S. K., X. Wang, D. J. Stensrud, and A. Johnson, 2018: Understanding the impact of radar and in situ observations on the prediction of a nocturnal convection initiation event on 25 June 2013 using an ensemble-based multiscale data assimilation system. *Mon. Wea. Rev.*, **146**, 1837–1859, https://doi.org/10.1175/MWR-D-17-0128.1.

Delgado, R., and K. Vermeesch, 2016: FP2 UMBC surface weather station data, version 1.0. UCAR/NCAR–Earth Observing Laboratory, accessed 1 June 2018, https://doi.org/10.5065/D6SJ1HSG.

Dowell, D. C., F. Zhang, L. J. Wicker, C. Synder, and N. A. Crook, 2004: Wind and temperature retrievals in the 17 May 1981 Arcadia, Oklahoma, supercell: Ensemble Kalman filter experiments. *Mon. Wea. Rev.*, **132**, 1982–2005, https://doi.org/10.1175/1520-0493(2004)132<1982:WATRIT>2.0.CO;2.

Du, J., and Coauthors, 2014: NCEP regional ensemble update: Current systems and planned storm-scale ensembles. *26th Conf. on Weather Analysis and Forecasting/22nd Conf. on Numerical Weather Prediction*, Atlanta, GA, Amer. Meteor. Soc., J1.4, https://ams.confex.com/ams/94Annual/webprogram/Paper239030.html.

Earth System Research Laboratory, 2016: The High-Resolution Rapid Refresh (HRRR). NOAA Earth System Research Laboratory, accessed 15 February 2017, https://rapidrefresh.noaa.gov/hrrr/.

Ek, M., K. Mitchell, Y. Lin, E. Rogers, P. Grunmann, V. Koren, G. Gayno, and J. Tarpley, 2003: Implementation of Noah land surface model advances in the National Centers for Environmental Prediction operational mesoscale Eta Model. *J. Geophys. Res.*, **108**, 8851–8867, https://doi.org/10.1029/2002JD003296.

Geer, A. J., and P. Bauer, 2011: Observation errors in all-sky data assimilation. *Quart. J. Roy. Meteor. Soc.*, **137**, 2024–2037, https://doi.org/10.1002/qj.830.

Geerts, B., and Coauthors, 2017: The 2015 Plains Elevated Convection At Night (PECAN) field project. *Bull. Amer. Meteor. Soc.*, **98**, 767–786, https://doi.org/10.1175/BAMS-D-15-00257.1.

Grant, B. N., 1995: Elevated cold-sector severe thunderstorms: A preliminary study. *Natl. Wea. Dig.*, **19**, 25–31.

Grell, G. A., and S. R. Freitas, 2013: A scale and aerosol aware stochastic convective parameterization for weather and air quality modeling. *Atmos. Chem. Phys.*, **13**, 23 845–23 893, https://doi.org/10.5194/acpd-13-23845-2013.

Haghi, K. R., and Coauthors, 2019: Bore-ing into nocturnal convection. *Bull. Amer. Meteor. Soc.*, **100**, 1103–1121, https://doi.org/10.1175/BAMS-D-17-0250.1.

Hanesiak, J., and D. Turner, 2016a: FP3 University of Manitoba Doppler lidar wind profile data, version 1.0. UCAR/NCAR–Earth Observing Laboratory, accessed 1 June 2018, https://doi.org/10.5065/D60863P5.

——, and ——, 2016b: FP6 University of Manitoba Doppler lidar VAD winds data, version 2.0. UCAR/NCAR–Earth Observing Laboratory, accessed 1 June 2018, https://doi.org/10.5065/D64F1NTN.

Hartung, D. C., J. A. Otkin, R. A. Petersen, D. D. Turner, and W. F. Feltz, 2011: Assimilation of surface-based boundary layer profiler observations during a cool-season weather event using an observing system simulation experiment. Part II: Forecast assessment. *Mon. Wea. Rev.*, **139**, 2327–2346, https://doi.org/10.1175/2011MWR3623.1.

Hitchcock, S. M., M. C. Coniglio, and K. H. Knopfmeier, 2016: Impact of MPEX observations on ensemble analyses and forecasts of the 31 May 2013 convective event over Oklahoma. *Mon. Wea. Rev.*, **144**, 2889–2913, https://doi.org/10.1175/MWR-D-15-0344.1.

Holdridge, D., and D. Turner, 2015: FP6 Hesston, KS radiosonde data, version 1.0. UCAR/NCAR–Earth Observing Laboratory, accessed 1 June 2018, https://doi.org/10.5065/D6765CD0.

Hong, S., and J. J. Lim, 2006: The WRF single-moment 6-class microphysics scheme (WSM6). *J. Korean Meteor. Soc.*, **42**, 129–151.

Horel, J., and Coauthors, 2002: Mesowest: Cooperative Mesonets in the western United States. *Bull. Amer. Meteor. Soc.*, **83**, 211–225, https://doi.org/10.1175/1520-0477(2002)083<0211:MCMITW>2.3.CO;2.

Horgan, K. L., D. M. Schultz, J. E. Hales, S. F. Corfidi, and R. H. Johns, 2007: A five-year climatology of elevated severe convective storms in the United States east of the Rocky Mountains. *Wea. Forecasting*, **22**, 1031–1044, https://doi.org/10.1175/WAF1032.1.

Houtekamer, P. L., and F. Zhang, 2016: Review of the ensemble Kalman filter for atmospheric data assimilation. *Mon. Wea. Rev.*, **144**, 4489–4532, https://doi.org/10.1175/MWR-D-15-0440.1.

Iacono, M. J., J. S. Delamere, E. J. Mlawer, M. W. Shephard, S. A. Clough, and W. D. Collins, 2008: Radiative forcing by long-lived greenhouse gases: Calculations with the AER radiative transfer models. *J. Geophys. Res.*, **113**, D13103, https://doi.org/10.1029/2008JD009944.

Johns, R. H., and C. A. Doswell, 1992: Severe local storms forecasting. *Wea. Forecasting*, **7**, 588–612, https://doi.org/10.1175/1520-0434(1992)007<0588:SLSF>2.0.CO;2.

Johnson, A., and X. Wang, 2017: Design and implementation of a GSI-based convection-allowing ensemble data assimilation and forecast system for the PECAN field experiment. Part I: Optimal configurations for nocturnal convection prediction using retrospective cases. *Wea. Forecasting*, **32**, 289–315, https://doi.org/10.1175/WAF-D-16-0102.1.

——, ——, J. R. Carley, L. J. Wicker, and C. Karstens, 2015: A comparison of multiscale GSI-based EnKF and 3DVar data assimilation using radar and conventional observations for midlatitude convective-scale precipitation forecasts. *Mon. Wea. Rev.*, **143**, 3087–3108, https://doi.org/10.1175/MWR-D-14-00345.1.

——, ——, and S. K. Degelia, 2017: Design and implementation of a GSI-based convection-allowing ensemble data assimilation and forecast system for the PECAN field experiment. Part II: Overview and evaluation of real-time system. *Wea. Forecasting*, **32**, 1227–1251, https://doi.org/10.1175/WAF-D-16-0201.1.

——, ——, K. R. Haghi, and D. B. Parsons, 2018: Evaluation of forecasts of a convectively generated bore using an intensively observed case study from PECAN. *Mon. Wea. Rev.*, **146**, 3097–3122, https://doi.org/10.1175/MWR-D-18-0059.1.

Kawabata, T., H. Seko, K. Saito, T. Kuroda, K. Tamiya, T. Tsuyuki, Y. Honda, and Y. Wakazuki, 2007: An assimilation and forecasting experiment of the Nerima Heavy Rainfall with a Cloud-Resolving Nonhydrostatic 4-Dimensional Variational Data Assimilation System. *J. Meteor. Soc. Japan*, **85**, 255–276, https://doi.org/10.2151/jmsj.85.255.

——, H. Iwai, H. Seko, Y. Shoji, K. Saito, S. Ishii, and K. Mizutani, 2014: Cloud-resolving 4D-Var assimilation of Doppler wind lidar data on a meso-gamma-scale convective system. *Mon. Wea. Rev.*, **142**, 4484–4498, https://doi.org/10.1175/MWR-D-13-00362.1.

Klein, P., D. Turner, E. Smith, and J. Gebauer, 2016: Mobile PISA 1 OU/NSSL CLAMPS radiosonde data, version 1.0. UCAR/NCAR–Earth Observing Laboratory, accessed 1 June 2018, https://doi.org/10.5065/D6416VDH.

Knupp, K., and R. Wade, 2016: MP2 UAH MIPS 915 MHz profiler NIMA-processed consensus wind and moments data, version 1.0. UCAR/NCAR–Earth Observing Laboratory, accessed 1 June 2018, https://doi.org/10.5065/D6B27SJ2.

Lakshmanan, V., T. Smith, G. Stumpf, and K. Hondl, 2007: The Warning Decision Support System-Integrated Information. *Wea. Forecasting*, **22**, 596–612, https://doi.org/10.1175/WAF1009.1.

Lin, Y., R. D. Farley, and H. D. Orville, 1983: Bulk parameterization of the snow field in a cloud model. *J. Climate Appl. Meteor.*, **22**, 1065–1092, https://doi.org/10.1175/1520-0450(1983)022<1065:BPOTSF>2.0.CO;2.

Loehrer, S. M., T. A. Edmands, and J. A. Moore, 1996: TOGA COARE upper-air sounding data archive: Development and quality control procedures. *Bull. Amer. Meteor. Soc.*, **77**, 2651–2672, https://doi.org/10.1175/1520-0477(1996)077<2651:TCUASD>2.0.CO;2.

Markowski, P., and Y. Richardson, 2010: *Mesoscale Meteorology in Midlatitudes*. Wiley-Blackwell, 430 pp.

Menzies, R. T., and R. M. Hardesty, 1989: Coherent Doppler lidar for measurements of wind fields. *Proc. IEEE*, **77**, 449–462, https://doi.org/10.1109/5.24130.

Minamide, M., and F. Zhang, 2017: Adaptive observation error inflation for assimilating all-sky satellite radiance. *Mon. Wea. Rev.*, **145**, 1063–1081, https://doi.org/10.1175/MWR-D-16-0257.1.

Morse, C. S., R. K. Goodrich, and L. B. Cornman, 2002: The NIMA method for improved moment estimation from Doppler spectra. *J. Atmos. Oceanic Technol.*, **19**, 274–295, https://doi.org/10.1175/1520-0426-19.3.274.

Nakanishi, M., and H. Niino, 2006: An improved Mellor–Yamada level-3 model: Its numerical stability and application to a regional prediction of advection fog. *Bound.-Layer Meteor.*, **119**, 397–407, https://doi.org/10.1007/s10546-005-9030-8.

National Research Council, 2009: *Observing Weather and Climate from the Ground Up: A Nationwide Network of Networks.* National Academies Press, 250 pp., https://doi.org/10.17226/12540.

Newsom, R. K., W. A. Brewer, J. M. Wilczak, D. E. Wolfe, S. P. Oncley, and J. K. Lundquist, 2017: Validating precision estimates in horizontal wind measurements from a Doppler lidar. *Atmos. Meas. Tech.*, **10**, 1229–1240, https://doi.org/10.5194/amt-10-1229-2017.

Otkin, J. A., D. C. Hartung, D. D. Turner, R. A. Petersen, W. F. Feltz, and E. Janzon, 2011: Assimilation of surface-based boundary layer profiler observations during a cool-season weather event using an observing system simulation experiment. Part I: Analysis impact. *Mon. Wea. Rev.*, **139**, 2309–2326, https://doi.org/10.1175/2011MWR3622.1.

Peters, J. M., E. R. Nielsen, M. D. Parker, S. M. Hitchcock, and R. S. Schumacher, 2017: The impact of low-level moisture errors on model forecasts of an MCS observed during PECAN. *Mon. Wea. Rev.*, **145**, 3599–3624, https://doi.org/10.1175/MWR-D-16-0296.1.

Privé, N. C., R. M. Errico, and K.-S. Tai, 2014: The impacts of increased frequency of rawinsonde observations on forecast skill investigated with an observing system simulation experiment. *Mon. Wea. Rev.*, **142**, 1823–1834, https://doi.org/10.1175/MWR-D-13-00237.1.

Reif, D. W., and H. B. Bluestein, 2017: A 20-year climatology of nocturnal convection initiation over the central and southern Great Plains during the warm season. *Mon. Wea. Rev.*, **145**, 1615–1639, https://doi.org/10.1175/MWR-D-16-0340.1.

Rogers, E., and Coauthors, 2009: The NCEP North American Mesoscale Modeling System: Recent changes and future plans. *23rd Conf. on Weather Analysis and Forecasting/19th Conf. on Numerical Weather Prediction*, Omaha, NE, Amer. Meteor. Soc., 2A.4, https://ams.confex.com/ams/23WAF19NWP/techprogram/paper_154114.htm.

Schwartz, C. S., and R. A. Sobash, 2017: Generating probabilistic forecasts from convection-allowing ensembles using neighborhood approaches: A review and recommendations. *Mon. Wea. Rev.*, **145**, 3397–3418, https://doi.org/10.1175/MWR-D-16-0400.1.

——, and Coauthors, 2010: Toward improved convection-allowing ensembles: Model physics sensitivities and optimizing probabilistic guidance with small ensemble membership. *Wea. Forecasting*, **25**, 263–280, https://doi.org/10.1175/2009WAF2222267.1.

Shao, H., and Coauthors, 2016: Bridging research to operations transitions: Status and plans of community GSI. *Bull. Amer. Meteor. Soc.*, **97**, 1427–1440, https://doi.org/10.1175/BAMS-D-13-00245.1.

Shapiro, A., E. Fedorovich, and S. Rahimi, 2016: A unified theory for the Great Plains nocturnal low-level jet. *J. Atmos. Sci.*, **73**, 3037–3057, https://doi.org/10.1175/JAS-D-15-0307.1.

Shin, H., and S.-Y. Hong, 2011: Intercomparison of planetary boundary-layer parameterizations in the WRF Model for a single day from CASES-99. *Bound.-Layer Meteor.*, **139**, 261–281, https://doi.org/10.1007/s10546-010-9583-z.

Sivaraman, C., L. Ma, L. Riihimaki, P. Muradyan, R. Coulter, S. Collis, and S. Xie, 1990: Radar wind profiler (915RWPPRECIPCON; updated hourly) from Southern Great Plains (SGP) central facility (C1), NW radar wind profiler site (I10), NE radar wind profiler site (8). Atmospheric Radiation Measurement (ARM) climate research facility data archive, accessed 1 June 2018, https://doi.org/10.5439/1025127.

Skamarock, W. C., and Coauthors, 2008: A description of the Advanced Research WRF Version 3. NCAR Tech. Note NCAR/TN-475+STR, 113 pp., https://doi.org/10.5065/D68S4MVH.

Smith, E. N., J. A. Gibbs, E. Fedorovich, and T. Bonin, 2015: WRF Model study of the Great Plains low-level jet: Effects of grid spacing and boundary layer parameterizations. *22nd Symp. on Boundary Layers and Turbulence*, Salt Lake City, UT, Amer. Meteor. Soc., 14B.1, https://ams.confex.com/ams/32AgF22BLT3BG/webprogram/Paper294866.html.

Smith, T. M., and Coauthors, 2016: Multi-Radar Multi-Sensor (MRMS) severe weather and aviation products: Initial operating capabilities. *Bull. Amer. Meteor. Soc.*, **97**, 1617–1630, https://doi.org/10.1175/BAMS-D-14-00173.1.

Sobash, R. A., and D. J. Stensrud, 2015: Assimilating surface mesonet observations with the EnKF to improve ensemble forecasts of convection initiation on 29 May 2012. *Mon. Wea. Rev.*, **143**, 3700–3725, https://doi.org/10.1175/MWR-D-14-00126.1.

Stelten, S., and W. A. Gallus, 2017: Pristine nocturnal convective initiation: A climatology and preliminary examination of predictability. *Wea. Forecasting*, **32**, 1613–1635, https://doi.org/10.1175/WAF-D-16-0222.1.

Storm, B., J. Dudhia, S. Basu, A. Swift, and I. Giammanco, 2009: Evaluation of the Weather Research and Forecasting Model on forecasting low-level jets: Implications for wind energy. *Wind Energy*, **12**, 81–90, https://doi.org/10.1002/we.288.

Sun, J., and S. B. Trier, 2018: Physical processes leading to elevated convection initiation during 25–26 June PECAN: Convective-scale reanalysis based on a radar data assimilation system. *Special Symp. on Plains Elevated Convection At Night (PECAN)*, Austin, TX, Amer. Meteor. Soc., 1.6, https://ams.confex.com/ams/98Annual/webprogram/Paper336167.html.

Surcel, M., M. Berenguer, and I. Zawadzki, 2010: The diurnal cycle of precipitation from continental radar mosaics and numerical weather prediction models. Part I: Methodology and seasonal comparison. *Mon. Wea. Rev.*, **138**, 3084–3106, https://doi.org/10.1175/2010MWR3125.1.

Tao, W.-K., and Coauthors, 2003: Microphysics, radiation and surface processes in the Goddard Cumulus Ensemble (GCE) model. *Meteor. Atmos. Phys.*, **82**, 97–137, https://doi.org/10.1007/s00703-001-0594-7.

Trier, S. B., and D. B. Parsons, 1993: Evolution of environmental conditions preceding the development of a nocturnal mesoscale convective complex. *Mon. Wea. Rev.*, **121**, 1078–1098, https://doi.org/10.1175/1520-0493(1993)121<1078:EOECPT>2.0.CO;2.

——, J. W. Wilson, D. A. Ahijevych, and R. A. Sobash, 2017: Mesoscale vertical motions near nocturnal convection initiation in PECAN. *Mon. Wea. Rev.*, **145**, 2919–2941, https://doi.org/10.1175/MWR-D-17-0005.1.

——, R. D. Roberts, J. Sun, T. M. Weckwerth, and J. W. Wilson, 2018: Physical processes influencing elevated convection initiation during 25–26 June PECAN: Observations and numerical simulations. *Special Symp. on Plains Elevated Convection At Night (PECAN)*, Austin, TX, Amer. Meteor. Soc., 1.5, https://ams.confex.com/ams/98Annual/webprogram/Paper335614.html.

Turner, D., 2016a: FP2 AERIoe thermodynamic profile retrieval data, version 1.0. UCAR/NCAR–Earth Observation Laboratory, accessed 1 June 2018, https://doi.org/10.5065/d6x63k9k.

——, 2016b: FP3 AERIoe thermodynamic profile retrieval data, version 2.0. UCAR/NCAR–Earth Observation Laboratory, accessed 1 June 2018, https://doi.org/10.5065/D6Z31WV0.

——, 2016c: FP5 AERIoe thermodynamic profile retrieval data, version 2.0. UCAR/NCAR–Earth Observation Laboratory, accessed 1 June 2018, https://doi.org/10.5065/D61V5C5J.

——, 2016d: FP6 ARM surface meteorology data, version 1.0. UCAR/NCAR– Earth Observing Laboratory, accessed 1 June 2018, https://doi.org/10.5065/D6RR1WN0.

——, 2016e: MP1 OU/NSSL CLAMPS Doppler lidar VAD wind data, version 1.0. UCAR/NCAR–Earth Observing Laboratory, accessed 1 June 2018, https://doi.org/10.5065/D6BR8QJH.

——, and U. Löhnert, 2014: Information content and uncertainties in thermodynamic profiles and liquid cloud properties retrieved from the ground-based Atmospheric Emitted Radiance Interferometer (AERI). *J. Appl. Meteor. Climatol.*, **53**, 752–771, https://doi.org/10.1175/JAMC-D-13-0126.1.

UCAR/NCAR, 2015a: FP1 ARM central facility radiosonde data, version 1. UCAR/NCAR–Earth Observation Laboratory, accessed 1 June 2018, https://data.eol.ucar.edu/dataset/485.021.

——, 2015b: FP3 FP4 FP5 QC 5 min surface data, tilt corrected, version 1.0. UCAR/NCAR–Earth Observing Laboratory, accessed 1 June 2018, https://doi.org/10.5065/D6BZ645V.

——, 2015c: FP4 NCAR/EOL 915 MHz profiler NIMA consensus winds and moments, version 1.0. UCAR/NCAR–Earth Observing Laboratory, accessed 1 June 2018, https://doi.org/10.5065/D6RV0KXH.

——, 2015d: FP5 NCAR/EOL 915 MHz profiler 30 minute consensus winds and moments data, version 1.0. UCAR/NCAR–Earth Observing Laboratory, accessed 1 June 2018, https://doi.org/10.5065/D6H993DQ.

——, 2016a: FP4 NCAR/EOL QC soundings, version 2.0. UCAR/NCAR–Earth Observing Laboratory, accessed 1 June 2018, https://doi.org/10.5065/D63776XH.

——, 2016b: FP5 NCAR/EOL QC soundings, version 2.0. UCAR/NCAR–Earth Observing Laboratory, accessed 1 June 2018, https://doi.org/10.5065/D6ZG6QF7.

——, 2016c: MP4 NCAR/EOL MISS 915 MHz profiler 30 minute consensus winds and moments and surface meteorology data, version 1.0. UCAR/NCAR–Earth Observing Laboratory, accessed 1 June 2018, https://doi.org/10.5065/D6RJ4GPJ.

——, 2016d: MP4 NCAR/EOL QC soundings, version 2.0. UCAR/NCAR–Earth Observing Laboratory, accessed 1 June 2018, https://doi.org/10.5065/D6707ZNV.

——, 2017: FP3 NCAR/EOL 449MHz profiler 30 minute consensus winds data, version 1.0 [PRELIMINARY]. UCAR/NCAR–Earth Observing Laboratory, accessed 1 June 2018, https://doi.org/10.5065/D66W98T7.

Vaisala, 2017: Vaisala Radiosonde RS41 Measurement Performance. Ref. B211356EN-B, 28 pp., https://www.vaisala.com/sites/default/files/documents/WEA-MET-RS41-Performance-White-paper-B211356EN-B-LOW-v3.pdf.

Vermeesch, K., 2015: FP2 Greensburg, KS radiosonde data, version 1.0. UCAR/NCAR–Earth Observation Laboratory, accessed 1 June 2018, https://doi.org/10.5065/D6FQ9TPH.

Wagner, T., D. Turner, and R. Newsom, 2016a: MP3 University of Wisconsin SPARC Doppler lidar VAD wind data, version 2.0. UCAR/NCAR–Earth Observing Laboratory, accessed 1 June 2018, https://doi.org/10.5065/D6V9869B.

——, E. Olson, N. Smith, and W. Feltz, 2016b: MP3 University of Wisconsin SPARC AERIoe thermodynamic profile data, version 1.0. UCAR/NCAR–Earth Observing Laboratory, accessed 1 June 2018, https://doi.org/10.5065/D60Z71HC.

——, ——, ——, and ——, 2016c: Mobile PISA 3 UW/SSEC SPARC radiosonde data, version 2.0. UCAR/NCAR–Earth Observing Laboratory, accessed 1 June 2018, https://doi.org/10.5065/D6VH5M7B.

——, ——, ——, and ——, 2016d: MP3 University of Wisconsin SPARC surface meteorological data, version 1.0. UCAR/NCAR–Earth Observing Laboratory, accessed 1 June 2018, https://doi.org/10.5065/D6N014XZ.

Wang, X., D. Parrish, D. Kleist, and J. Whitaker, 2013: GSI 3DVar-based ensemble–variational hybrid data assimilation for NCEP Global Forecast System: Single-resolution experiments. *Mon. Wea. Rev.*, **141**, 4098–4117, https://doi.org/10.1175/MWR-D-12-00141.1.

Wang, Y., and X. Wang, 2017: Direct assimilation of radar reflectivity without tangent linear and adjoint of the nonlinear observation operator in the GSI-based EnVar system: Methodology and experiment with the 8 May 2003 Oklahoma City tornadic supercell. *Mon. Wea. Rev.*, **145**, 1447–1471, https://doi.org/10.1175/MWR-D-16-0231.1.

Waugh, S., and C. Ziegler, 2017: NSSL mobile mesonet data, version 1.1. UCAR/NCAR–Earth Observing Laboratory, accessed 1 June 2018, https://doi.org/10.5065/D64M92RG.

Wei, M., Z. Toth, R. Wobus, and Y. Zhu, 2008: Initial perturbations based on the ensemble transform (ET) technique in the NCEP global operational forecast system. *Tellus*, **60A**, 62–79, https://doi.org/10.1111/j.1600-0870.2007.00273.x.

Weisman, M. L., C. Davis, W. Wang, K. W. Manning, and J. B. Klemp, 2008: Experiences with 0–36-h explicit convective forecasts with the WRF-ARW Model. *Wea. Forecasting*, **23**, 407–437, https://doi.org/10.1175/2007WAF2007005.1.

Wheatley, D. M., N. Yussouf, and D. J. Stensrud, 2014: Ensemble Kalman filter analyses and forecasts of a severe mesoscale convective system using different choices of microphysics schemes. *Mon. Wea. Rev.*, **142**, 3243–3263, https://doi.org/10.1175/MWR-D-13-00260.1.

Whitaker, J. S., T. M. Hamill, X. Wei, Y. Song, and Z. Toth, 2008: Ensemble data assimilation with the NCEP Global Forecast System. *Mon. Wea. Rev.*, **136**, 463–482, https://doi.org/10.1175/2007MWR2018.1.

Wilson, J. W., S. B. Trier, D. W. Reif, R. D. Roberts, and T. M. Weckwerth, 2018: Nocturnal elevated convection initiation of the PECAN 4 July hailstorm. *Mon. Wea. Rev.*, **146**, 243–262, https://doi.org/10.1175/MWR-D-17-0176.1.

Wulfmeyer, V., H. Bauer, M. Grzeschik, A. Behrendt, F. Vandenberghe, E. V. Browell, S. Ismail, and R. A. Rerrare, 2006: Four-dimensional variational assimilation of water vapor differential absorption lidar data: The first case study within IHOP_2002. *Mon. Wea. Rev.*, **134**, 209–230, https://doi.org/10.1175/MWR3070.1.

Zhang, J., and Coauthors, 2016: Multi-Radar Multi-Sensor (MRMS) quantitative precipitation estimation: Initial operating capabilities. *Bull. Amer. Meteor. Soc.*, **97**, 621–638, https://doi.org/10.1175/BAMS-D-14-00174.1.

Ziegler, C., M. Coniglio, M. Parker, and R. Schumacher, 2016: CSU/NCSU/NSSL MGAUS radiosonde data, version 3.0. UCAR/NCAR–Earth Observing Laboratory, accessed 1 June 2018, https://doi.org/10.5065/D6W66HXN.